



1 **Improved subglacial boundary conditions near Dome C, Antarctica, through**
2 **rigorous integration of multi-campaign radar data and an ensemble stochastic**
3 **simulation approach**

4 *Calvin Shackleton*^{1*}, *Kenichi Matsuoka*¹, *Brett Fraysher*², *Joochan Lee*³, *Jørgen Dall*⁴, *Allain Rapadas*²,
5 *Prasad Gogineni*², *Drew Taylor*², *Hyeon Tae Ju*³, *Changhyun Chung*³, *Anders Kusk*⁴

6 *calvin.shackleton@npolar.no

7 ¹Norwegian Polar Institute, Fram Senteret, Tromsø, Norway

8 ²University of Alabama, Tuscaloosa, Alabama, USA

9 ³Korean Polar Research Institute, Incheon, Korea

10 ⁴DTU Space, Technical University of Denmark, Lyngby, Denmark

11

12

13 **Abstract**

14 Subglacial bed topography is a fundamental boundary condition for ice-sheet flow, basal thermal
15 regimes, and the preservation of palaeoclimate records, yet it remains highly uncertain across
16 Antarctica. We use stochastic simulation methods to generate an ensemble of gridded (500 m) ice
17 thickness and bed elevation near Dome C, and map bed elevation uncertainty accounting for impacts of
18 data availability and basal roughness. New airborne radar measurements uncover previously
19 undocumented sectors of the ice-bed interface and we integrate these with existing data using a rigorous
20 approach to ensure nearby measurement compatibility. Our simulated bed shows improved
21 representation of basal roughness between survey profiles, revealing regional roughness over 50% higher
22 than previous interpolations. We apply the ensemble to investigate uncertainty in meltwater routing,
23 identifying well-constrained drainage away from the Dome C Plateau but poorly constrained outflow
24 from Concordia Lake and parts of the Belgica Highlands. Topographic focussing of geothermal heat
25 predicts local anomalies up to $\pm 30\%$ relative to the regional value, and several ice core drill sites are in a
26 zone of 12% locally-reduced geothermal heating which is favourable for deep ice layer preservation. This
27 work demonstrates that the critical subglacial bed boundary condition is better represented by
28 ensemble-based, stochastic simulations based on strictly cross-validated data rather than single
29 deterministic interpolations, and simulated beds can improve the reliability of analyses with robust
30 consideration of uncertainties in data-sparse regions.

31

32

33

34

35

36

37

38

39

40

41



42 1. Introduction

43 Kilometer-scale subglacial topography influences basal thermal state through locally variable
 44 pressure-melting (Cuffey & Paterson, 2010) and also modulates the effective area for geothermal heat
 45 conduction (van der Veen et al., 2007). While basal roughness can be constrained in high resolution in
 46 the along-track orientation of radar profiles, this information is missing between survey profiles. Widely-
 47 used interpolation methods such as kriging and splines do not preserve the spatial statistics of
 48 measurements in data gaps, leading to over-smoothing in gridded products and unrealistic patterns in
 49 basal roughness. To preserve roughness characteristics in interpolated grids, Sequential Gaussian
 50 Simulation (SGS) can be applied to simulate values between measurements based on the values and
 51 variability of nearby data (Deutsch & Journel, 1997). This approach has been applied to generate
 52 ensembles of equally-likely bed elevation grids to investigate the basal environment, subglacial
 53 meltwater drainage, and geothermal heat flow (GHF) with robust consideration of the impacts of
 54 topographic uncertainty and realistic basal roughness (MacKie et al., 2020; MacKie et al., 2021;
 55 Shackleton et al., 2023).

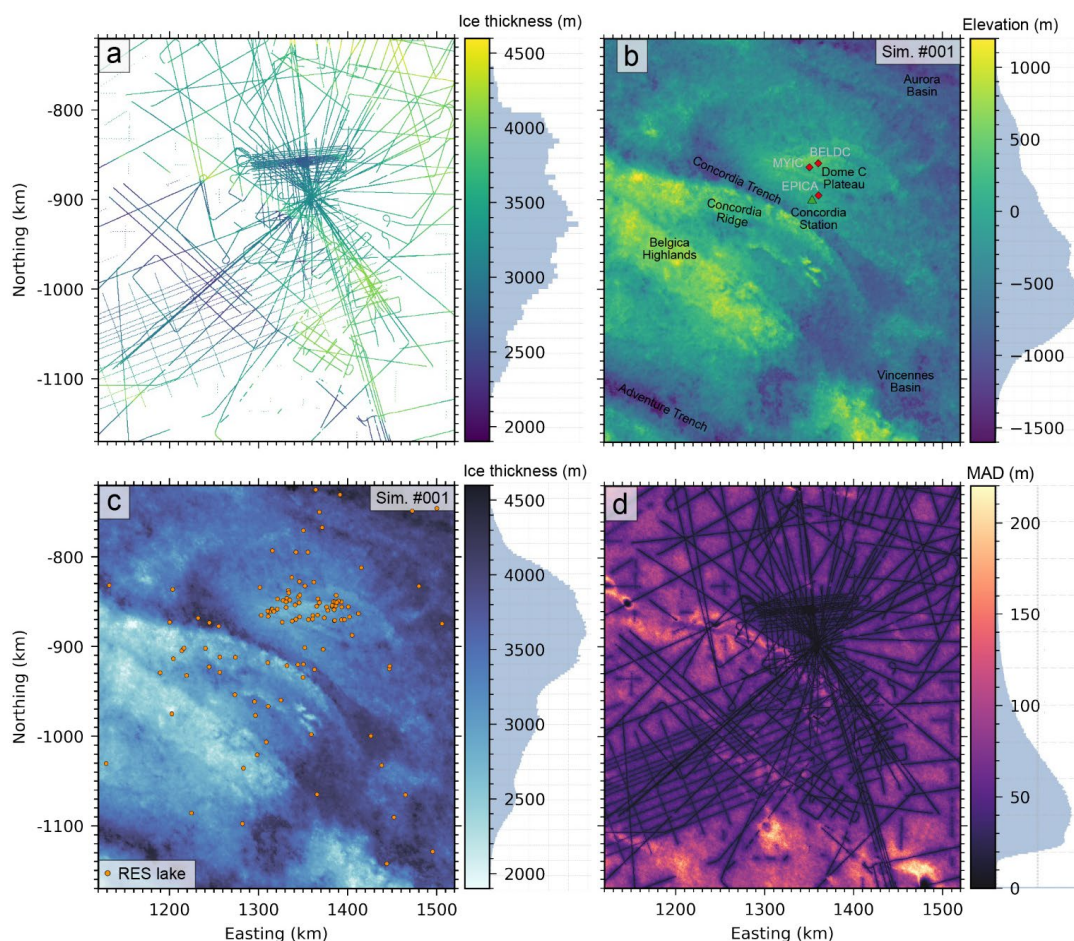


Figure 1: Region map, radar survey data, and simulation results. **a)** Radar-derived ice thickness measurements in the Dome C region. **b)** Simulated bed elevation #001 from the ensemble of 100, with Concordia Station (green triangle) and ice cores plotted (red square). **c)** Simulated ice thickness #001 from the ensemble of 100, with subglacial lakes (orange circle) inferred from compiled radio-echo sounding (RES) analyses (Livingstone et al., 2022). **d)** Median Absolute Deviation over the ensemble of 100 simulated bed elevation grids. All maps are projected to EPSG:3031.



56 Subglacial topography around Dome C is of particular interest in the context of paleoclimate
57 investigations. Oxygen isotope records from marine sediment cores indicate that global glacial-
58 interglacial cycles experienced a major shift in periodicity from 41 Ka to ca. 100 Ka between 1.4 Ma and
59 800 Ka BP (Lisiecki & Raymo, 2005). The underlying mechanisms for this Mid-Pleistocene Transition
60 (MPT) are not yet fully constrained (Berends et al., 2021), but deep ice cores that preserve atmospheric
61 gases from the palaeo-climate could provide continuous, high-resolution climate records. Ice layers that
62 span the last 1.5 Ma could be located near the base of thick ice domes in the interior of Antarctica,
63 though basal melting, ice flow, and accretion should be minimal to preserve ice layer stratigraphy
64 (Fischer et al., 2013; Van Liefferinge & Pattyn, 2013). To locate basal ice with undisturbed stratigraphy
65 and sufficient age resolution spanning the MPT, the ice core community are trying to delineate sites with:
66 1) ice around 2500 m thick, sufficient to resolve the MPT without inducing significant basal-melting; 2)
67 low surface accumulation to limit vertical strain-induced thinning of ice layers; 3) low basal roughness to
68 prevent disruption of basal ice stratigraphy through lateral strain; 4) low GHF to restrict basal melting and
69 preserve the oldest ice layers. The European Project for Ice coring in Antarctica (EPICA) successfully
70 retrieved a 3260 m long ice core near Dome C, Antarctica that provides climate records for the last 800
71 Ka (Jouzel et al., 2007; Lüthi et al., 2008).

72 Ice thickness, basal roughness, and GHF are critical boundary conditions for thermomechanical
73 modelling which delineate promising drill sites in the Dome C region that could resolve the MPT (Chung
74 et al., 2023b; Parrenin et al., 2017; Passalacqua et al., 2017; Van Liefferinge et al., 2018; Wang et al.,
75 2023; Young et al., 2017). Subglacial topography and ice thickness variability near Dome C (Fig. 1a-c) is
76 documented in radar surveys (Drewry et al., 1982; Forieri et al., 2004; Tabacco et al., 1998), with thinner
77 ice (<2.5 km) observed over the Belgica Highlands and Concordia Ridge, and 2.5-3.5 km thick ice over
78 the Dome C plateau. Ice thicknesses over 4 km are located above Concordia and Vincennes subglacial
79 lakes and in the Concordia Trench, with up to 4.7 km reported in the Aurora Subglacial Basin. The
80 Concordia Trench and Adventure Trench are tectonic features 20 – 50 km in width with over 1 km thicker
81 ice than the surroundings, oriented approximately northeast - southwest (Cianfarra et al., 2009). Spatial
82 coverage of surveys varies from the well-resolved topography over the Dome C plateau and surrounding
83 Concordia Station, to large data gaps over Vincennes Basin and southwest Belgica Highlands (Fig.1).

84 A large database of Antarctic radar-derived ice thickness measurements from surveys conducted
85 between 1966 and 2022 was compiled recently by the Bedmap project (Frémand et al., 2023), and
86 subsequent radar campaigns provide new measurements across key sites in the Dome C region to
87 improve characterization of the basal environment (Chung et al., 2023a; Mulvaney et al., 2023). In this
88 work, we integrate existing radar-derived ice thicknesses reported to the Bedmap database with
89 subsequently released data as well as new radar survey measurements over the Belgica Highlands
90 conducted by the Korean Polar Research Institute (KOPRI) and University of Alabama (UA) as well as over
91 the Dome C Plateau by the Technical University of Denmark (DTU). This data integration was carried out
92 using a robust filtering approach to minimize locally conflicting measurements in the compiled data. We
93 use measurements in a 400 x 400 km² region surrounding Dome C (Fig. 1a) to simulate an ensemble of
94 100 bed elevation and ice thickness grids using SGS. The results for simulation #001 out of the ensemble
95 are shown in Figure 1b and 1c as an illustrative example. By calculating variability over the ensemble we
96 also map out regional topographic uncertainty (Fig. 1d). The simulated bed topography is used to
97 investigate basal roughness, subglacial meltwater drainage, local topographic modification of GHF, and
98 we discuss the implications of findings for the preservation of deep ice layers.

99

100

101



102 **2. Data compilation, quality control, and methodology**

103 **2.1 Radar-derived ice thickness data**

104 We compiled available radar measurements of two-way travel time (TWT) from the ice surface to ice-
105 bed interface from surveys conducted near Dome C, totalling ca. 2.3 million data points (Fig. 1a). For all
106 compiled TWT data, ice thicknesses were calculated assuming a radar wave propagation speed in ice of
107 $169 \text{ m } \mu\text{s}^{-1}$ and no firn corrections. The data compilation included new airborne surveys by a 2023/2024
108 Korean Polar Research Institute (KOPRI) and University of Alabama (UA) collaboration as well as a
109 2024/2025 survey by The Technical University of Denmark (DTU), 2016-2018 and 2019-2020 ground
110 surveys from the Beyond EPICA - Oldest Ice (BE-OI) project, and ice thickness measurements with
111 multiple sources from the Bedmap3 database:

112 *2.1.1 KOPRI/UA airborne survey*

113 A new 2023-2024 airborne survey from a KOPRI-UA collaboration provided 960 km lines of
114 georeferenced radar data used to pick ice-bed TWT. These data were collected with a multi-channel
115 ultra-wideband (UWB) ice-penetrating radar designed to operate over a frequency range of 170-470 MHz.
116 The system consists of 8 transmit channels and 8 receive channels. Each transmit channel is supplied
117 with chirped pulses of about 200 W of peak power. The radar is operated with a short pulse of 1-3 μs
118 duration to sound shallow ice and map internal layers to a depth of 1000 m, and a long pulse of 5-10 μs
119 duration to sound thicker ice and map deeper layers. The system consists of a 16-element transmit array
120 mounted under the left wing and a 16-element receive array mounted under the right wing. Two transmit
121 and two receive channels are combined using a power divider/combiner to operate with a single transmit
122 and receive channel. A more detailed system description is available in Awasthi et al. (2022) and Rizvi et
123 al. (2025).

124 During this airborne campaign in 2023, we could not operate the system with its full bandwidth and
125 power. One of the two inverters supplying power to the radar system from the aircraft failed. This led us to
126 limit the number of channels, the operating frequency range (170-230 MHz), and the pulse width, so the
127 radar could operate with only one inverter. Despite this constraint, the system maintained sufficient
128 power and capability to recover bed echoes and internal stratigraphy across the region, demonstrating
129 its ability to reconfigure to meet field and logistical constraints.

130 Data processing consisted of six major steps: 1) reduction of any coherent noise caused by the
131 system or external sources; 2) pulse compression to improve range resolution and improve signal-to-
132 noise ratio (Skolnik, 2008); 3) motion compensation to reduce errors introduced by aircraft flight path
133 deviations; 4) synthetic aperture processing using a frequency-wavenumber (f-k) migration algorithm
134 (Stolt, 1978) to improve both along-track resolution and signal-to-noise ratio; 5) correction of amplitude
135 and phase differences between channels, and 6) combination of data from all channels and reduction of
136 speckle using a reduction filter to improve image interpretation (Lee et al., 1994). Steps 1-4 were applied
137 to each channel of received data, and processed data are then equalized and combined, with the
138 additional image processing applied to the final image.

139 *2.1.2 DTU airborne survey*

140 A new 2024 airborne survey by DTU using the POLarimetric Airborne Radar Ice Sounder (POLARIS)
141 system (Dall et al., 2010), provided ca. 1 million latitude, longitude, ice surface elevation, and TWT data
142 points that spanned ca. 772 line km of survey profiles. Commissioned by ESA, DTU developed the
143 POLARIS radar, which can be in-flight configured for acquisition of either sounder data or synthetic
144 aperture radar (SAR) data (Dall et al., 2013) at a center frequency of 435 MHz (P-band). With a maximum
145 bandwidth of 85 MHz, a vertical resolution down to about 1 m in ice can be achieved, but in order to



146 improve the sensitivity to vertically distributed reflectors (e.g. internal layers), the Dome C data were
147 acquired in a shallow/deep sounding mode, where a reduced bandwidth (30 MHz), a larger pulse length,
148 and a higher receiver gain was used for the lower of two overlapping depth windows. The two depth
149 windows were covered in a pulse-interleaved fashion, and the shorter pulse length that was used for
150 shallow sounding enabled a lower flight altitude, hence less surface clutter. The POLARIS configuration
151 prioritized polarimetry over coherent clutter suppression (Nielsen and Dall, 2015).

152 GNSS data and IMU data were acquired with an iMAR iNAT-M200-SLN navigation unit, PPP-processed
153 with Waypoint Inertial Explorer, and used for motion compensation and geocoding. Narrowband RFI was
154 masked out, and wideband RFI was suppressed by replacing the impacted pulses with interpolated
155 pulses computed from highly correlated neighboring pulses. Upon range compression and along-track
156 focusing with a time-domain backprojection algorithm (Kusk and Dall, 2010), the POLARIS data were
157 calibrated using data from an internal calibration loop and external calibration adjustments derived from
158 POLARIS SAR data acquired over a trihedral radar reflector deployed near Casey Station. In this way both
159 intensity and time delay was calibrated. Speckle and a potential birefringence loss was reduced by
160 computing the span of the polarimetric covariance matrix and multi-looking by a factor of 5 in the along-
161 track direction. The ice surface and bed were traced in a semi-automatic manner with an algorithm
162 finding the depth where the leading edge of the return waveform has the steepest intensity slope.

163 2.1.3 *BE-OI ground surveys*

164 Ice thickness measurements from two ground surveys: a 2019-2020 survey near Little Dome C (LDC)
165 consisting of 12 profiles over an area of 5x8 km² using a very high frequency (VHF) multi-channel
166 coherent radar depth sounder (Chung et al., 2023a); a 2016-2018 survey using the Deep Looking radio
167 echo sounder (DELORES) from British Antarctic Survey (BAS) consisting of 116 radar profiles near LDC
168 and 21 profiles at North Patch covering an area of 5x5 km² (Mulvaney et al., 2023).

169 2.1.4 *Bedmap Database*

170 Ice thickness data from the Bedmap Database comprise radar-derived ice thickness measurements
171 from many surveys (*Table A1*) between 1966 and 2018 (Frémand et al., 2023) and provided 1.9 million
172 data points in the Dome C region. If not provided in the data files we calculated TWT from ice surface to
173 the ice-bed interface using wave propagation speed and firn corrections described in the survey source
174 reference.

175

176 2.2 Measurement consistency and data filtering

177 Nearby radar-derived ice thickness measurements can be inconsistent due to a combination of
178 factors, including off-nadir reflections from steep or rough bed topography and signal attenuation or
179 scattering in warm or debris-rich ice. To robustly calculate and model spatial variability in ice thickness
180 any inconsistencies between nearby measurements need to be minimized; large differences in ice
181 thickness could lead to overestimated variance. However, it is important to preserve as many data points
182 as possible when filtering, especially in data-sparse regions.

183 We conducted a thorough analysis of measurement consistency to identify surveys or locations with
184 significant differences within 50 m, which is less than the width of the first Fresnel zone for the regional
185 minimum ice thickness (60 m at ca. 2100 m depth). We identified 43,337 sites which had measurements
186 within a 50 m window that were not from the same radar profile. A large portion of these sites were from
187 nearby sub-parallel profiles, repeated survey tracks, or duplicated data in the Bedmap Database.
188 Appendices Figures A1-18 show the consistency between each of the 18 surveys and all other surveys in



189 the Dome C region. Although the differences between nearby data points from different surveys had a
 190 median of -1 m and standard deviation of 60 m, large and widespread inconsistencies in measured ice
 191 thickness with absolute differences up to 1324 m were identified (Fig. 2).

192 This analysis was used as a basis for filtering out a total of 275,677 incompatible data points. Overall,
 193 we aimed to have a strict filtering procedure to minimize nearby data with large inconsistencies that would
 194 impact the spatial statistics of ice thickness variability. If possible, we filtered out older data that could be
 195 lacking accurate GPS positioning where newer data was available. Details of the filtering steps applied to
 196 individual surveys are given in Table A1. The filtering was applied in four stages:

- 197 1. Filtering out locally inconsistent survey segments and duplicated data from specific surveys within
 198 0.2 km, with inconsistent surveys identified through manual inspection (Fig. A1-18) and preferred
 199 survey chosen based on lowest mean absolute differences between all other surveys. [removed
 200 98,176 data points]
- 201 2. Filtering data within a 0.6 km radius of large proximity errors (>50 m), performed sequentially for
 202 each survey and ordered based on averaged mean absolute differences between the survey and
 203 all other surveys. [removed 143,707 data points]
- 204 3. Filtering all data points from surveys before 1990 with no GPS positioning and potentially uncertain
 205 locations that are within 10 km of more recent surveys with reliable positioning. [removed 7963
 206 data points]
- 207 4. Filtering out data points along manually supplied sections of specific surveys where nearby
 208 measurement inconsistencies are large but could not be removed using automated filters.
 209 [removed 25,831 data points]

210

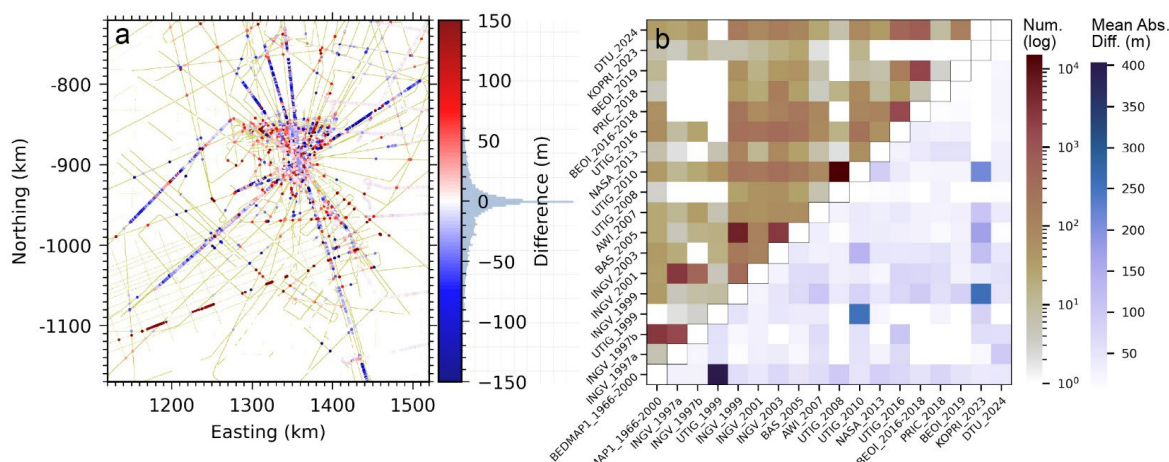


Figure 2: Measurement compatibility analysis. **a)** Difference in radar-derived ice thickness measurements (all data: small yellow points) between different surveys if available within a 50 m radius (Red-Blue coloured points show measurement difference). The colormap histogram shows the distribution of differences and is capped at ±150 m, though minimum difference is -655 m and maximum difference is 1324 m. **b)** Heatmap matrix of inconsistencies, with number of crossover sites (red) in upper left and mean absolute differences for each survey combination (blue) in lower right. Table A1 lists all radar profiles used in this study and filtering steps applied.

211

212

213

214



215 2.3 Spatial variability of filtered ice thickness data

216 The distance to the nearest measurement calculated for each grid cell in the simulation domain had
 217 a median of 2.2 km and standard deviation of 3.9 km, with a maximum distance of 34.1 km. We therefore
 218 aimed to calculate and model spatial relationships between measurements for a maximum lag distance
 219 of 40 km. We first decimated the radar-derived ice thickness measurements using a median reduction
 220 filter and gridded data to uniform 500 m spacings aligned to the Antarctic stereographic EPSG: 3031 grid
 221 using tools from the *Verde* python package (Uieda, 2018). This reduced the number of data points from
 222 ca. 2.3 million to ca. 61.5 thousand. Our median-decimated ice thickness measurements show that
 223 large-scale structure varies across different azimuths (Fig. 1a). To emphasize the relationships at shorter
 224 lag distances and minimize the variogram being impacted by large-scale structures, we modelled and
 225 removed these using a gaussian filter with a smoothing radius of 20 km (Fig. 3a), proceeding with the
 226 residual values (Fig. 3b) and storing modelled large-scale structures to be later added back onto
 227 simulated values. To facilitate a gaussian simulation process we normalised residual values to give a
 228 mean of 0 and standard deviation of 1, then computed the experimental variogram for 40 lag intervals
 229 with a separation of 1 km (Fig. 3c).

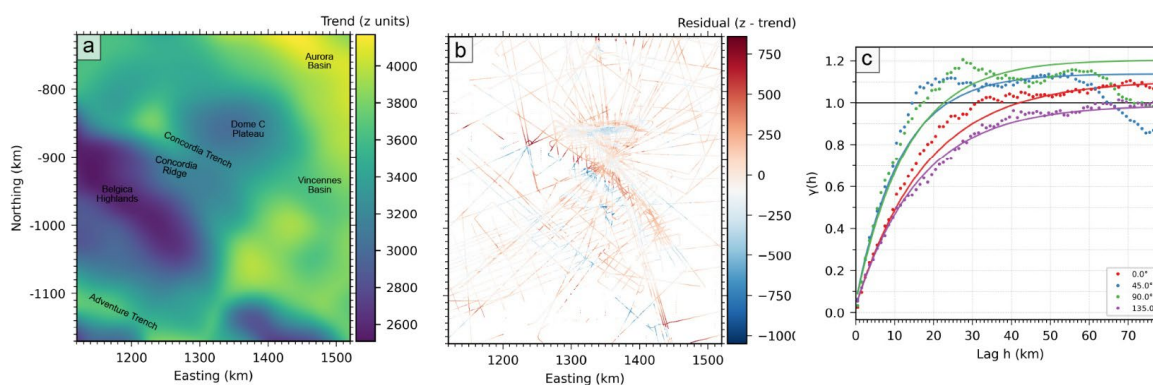


Figure 3: Large-scale, smoothed topography model and measurement variograms. **a)** Large-scale elevation trend modelled using a gaussian filter with 20 km radius, **b)** Residuals after removing the regional trend from data, **c)** Experimental and modelled variogram for normalised ice thickness values for four different azimuths relative to the Polar Stereographic projection. Each azimuth represents a band $\pm 22.5^\circ$ of the central value.

230

231 Despite removing large-scale ice thickness features, directional differences in variability can still
 232 be observed in the detrended data (Fig. 3b). To more accurately model spatial variability accounting for
 233 azimuthal differences, we calculated directional variograms across grid azimuths centered at 0° , 45° ,
 234 90° , 135° (Fig. 3c) relative to Polar Stereographic projected axes, which should be sufficient for data
 235 aligned on a grid. All azimuths referred to herein are grid based, not geographical. The directional
 236 variograms show measurement variance diverges even at short lag distances, rising sharply for azimuths
 237 of 45° and 90° and levelling off at a range of ca. 35 km. Variance for azimuths of 0° and 135° rise more
 238 slowly, and these also diverge for lag distances more than 10 km, with the 135° azimuth levelling off after
 239 50 km. We used the linear-weighted residual sums from a least-squares function applied to exponential,
 240 spherical, and Gaussian model fits to programmatically identify a best-fitting model type and parameters
 241 that can characterise the experimental variograms, prioritizing shorter lag distances and azimuths with
 242 the least variance. The experimental variogram at an azimuth of 135° shows the strongest continuity and
 243 is characterised well by an exponential model with a range of 50 km and a sill of 1.0 (Fig. 3c). The least
 244 continuity is observed for azimuths of 45° and 90° which are characterised by an exponential model with
 245 a range 35 - 39 km and sill of 1.1 - 1.2, especially at lag distances < 10 km and > 30 km (Fig. 3c).



246 **2.4 Stochastic simulation of ice thickness**

247 We used Sequential Gaussian Simulation (SGS) (Deutsch & Journel, 1997) to simulate ice
248 thicknesses based on code adapted from the *gstatsim* python package (MacKie et al., 2023). The
249 algorithm operated over a randomized path over our domain grid to sequentially simulate values based
250 on nearby data and modelled variance. For each unsimulated cell the algorithm builds a conditioning set
251 from nearby measurements, including any previously simulated values, and selects a maximum of 240
252 values within a radius of 50 km. The algorithm samples evenly from each of 8 octants if measurements
253 exist within the search radius and populates the set with the nearest data otherwise.

254 A local mean is estimated through kriging of distance-weighted nearby values, and variance is
255 determined from the covariance matrix for nearby data and the covariance function with model type and
256 parameters identified by the variogram model. Anisotropy is propagated into the simulation by inverse-
257 scaling distances used in the covariance functions based on the variogram range for the least-variable
258 and most-variable azimuths, respectively 135° and 45° with ranges 50 km and 35 km (Fig. 3c). A value is
259 selected at random for each grid cell from a Gaussian distribution drawn with centre at the local mean
260 and variance estimate for the most relevant lag distance. Once all grid cells were simulated, we
261 transformed the values from normalized space back into ice thicknesses and added back the modelled
262 large-scale ice thickness trends. An ensemble of 100 equally-likely ice thickness grids were simulated.

263

264 **2.5 Bed elevation grids, uncertainties, and meltwater routing**

265 We estimated 100 bed elevation grids by subtracting each of the 100 simulated ice thickness grids
266 from the Reference Elevation Model of Antarctica (REMA) ice surface elevations (Howat et al., 2019). To
267 evaluate short-scale bed roughness in the Dome C region we calculated the standard deviation within a
268 2 km radius of each grid cell (Taylor et al., 2004) for each simulated bed, calculating the mean over the
269 ensemble as well as for the Bedmap3 (Pritchard et al., 2025) and Bedmachine v4 (Morlighem, 2026)
270 interpolations. The median absolute deviation (MAD) over the ensemble of simulated bed elevation grids
271 was used to estimate topographic uncertainty, accounting for both distance from measurements and
272 bed roughness (Shackleton et al., 2023).

273 We also predicted subglacial meltwater flow directions and hydraulic basins using *pysheds* (Bartos,
274 2020) to fill sinks and calculate D8 flow directions for subglacial hydraulic potential, $\varphi = \rho_w g z + k \rho_i g h$
275 (Shreve, 1972), where ρ_w and ρ_i are the density of water and ice (kg m^{-3}), g is gravitational acceleration
276 (m s^{-2}), z and h are ensemble simulated bed elevations and ice thicknesses. We assume uniform basal
277 melting and that the ratio between subglacial water pressure and ice overburden pressure, k , is equal to
278 1. Stream and basin probability was calculated from averaged stream locations over the ensemble.

279

280 **3. Results**

281 **3.1 Simulated ice thickness and bed elevation**

282 We simulated an ensemble of 100 ice thickness and bed elevation grids for a 400x400 km² region
283 surrounding Dome C from 1120 km to 1520 km Easting, and -1170 km to -720 km Northing on an EPSG:
284 3031 Antarctic Sterographic projection. The full ensemble of simulated surfaces can be viewed in
285 *Appendix animation A*, which shows that values near measurements remain consistent across the
286 ensemble, whereas away from measurements values vary between simulations, increasingly with both
287 distance from measurements and local bed roughness. Simulation #001 is shown in *Figures 1b* and *1c*,
288 which confirms that large-scale structures such as northwest-southeast oriented bands of thicker and
289 thinner ice observed in radar data (e.g. Concordia Ridge; Fig. 1a) are represented well. Topographic
290 features 10's of kilometres in length are also resolved and are consistent across the ensemble in regions



291 with high data density, such as the 3 patches of low ice thickness near 1350 km Easting, -960 km
292 Northing. Features of this scale can shift in location over the ensemble for low data density regions in the
293 southwest and north of the domain. Small-scale topography below 5 km varies significantly over the
294 ensemble in all regions except in the central region where data density is the highest surrounding the ice
295 core sites (Fig. 1a). The simulations incorporate new measurements from a KOPRI-UA airborne radar
296 survey over the Belgica Highlands to the southwest of Concordia Station, documenting the southeast
297 extent of the Belgica Highlands and Concordia Ridge with increased detail and revealing bed elevations
298 more than 300 m higher than estimated from sparse data in previous interpolations (Bedmap 3: Pritchard
299 et al., 2025; Bedmachine v4: Morlighem, 2026).

300

301 **3.2 Bed elevation uncertainty**

302 The Median Absolute Deviation (MAD) over the ensemble of 100 simulated bed elevation grids
303 quantifies spatial uncertainties attributed to the combined influence of measurement density and basal
304 roughness in the Dome C region (Fig. 1d). The domain mean is 53 m with standard deviation of 32 m, and
305 lowest MAD near measurements, especially in high data density regions near Concordia Station. The
306 highest MAD is observed far from data, reaching a maximum of 260 m to the grid southeast. The primary
307 pattern in MAD follows the radar survey tracks, but secondary patterns are observed with grid northwest-
308 southeast trending bands of higher MAD aligned with the 10's of km scale troughs in the grid southwest
309 and northwest. Regions of higher MAD are also observed for relatively uniform radar survey spacings, for
310 example the band near 1300 km Easting, -1040 km Northing which is 60 m higher than the surroundings,
311 which also correlates with rougher terrain in simulated bed. Over the Dome C Plateau MAD reaches a
312 maximum of 60 m despite relatively dense radar data with maximum 4 km spaced surveys. However,
313 within several kilometres of the Million Year Ice Core (MYIC) and Beyond EPICA Little Dome C (BELDC)
314 ice core sites data is dense enough to constrain topographic uncertainty to 0 at the 500 m grid cell scale
315 of our simulations.

316

317 **4. Discussion**

318 Gridded representations of subglacial bed topography are fundamental boundary conditions for ice
319 sheet models and underpin a wide range of glaciological analyses. For modelling purposes, adequate
320 representation of basal roughness should be prioritised for realistic constraints on basal shear stress.
321 Although the impact of shear heating is likely to be small beneath ice domes due to low flow velocities,
322 the basal thermal state could be sensitive to small changes since much of the basal ice is at or near the
323 pressure-melting point. Replacing smooth bed with realistically rough topography was shown to improve
324 modelled basal ice motion and replicate temperate ice layer thicknesses observed in Greenland
325 boreholes (Law et al., 2023). In the context of ice core investigations, rougher basal topography can also
326 lead to deformation of basal ice layers which disrupts the continuity of deep ice stratigraphy. Provided
327 that all other conditions for locating old ice layers with undisturbed stratigraphy are also met (cf. Fischer
328 et al., 2013) it is therefore favourable to choose sites with relatively smooth basal topography when
329 selecting potential drill sites for old ice cores. We discuss our simulated bed topography results in the
330 context of basal roughness (Section 4.1), subglacial meltwater drainage (Section 4.2), and geothermal
331 heat flow (Section 4.3).

332

333

334



335 **4.1 Basal roughness**

336 We calculated standard deviations within a 2 km radius of each grid cell, σ_{2km} , as a measure of basal
 337 roughness (Taylor et al., 2004) for each of our ensemble simulated bed (Fig. 4a: Sim #001), as well as the
 338 Bedmap 3 interpolation (Fig. 4b) (Pritchard et al., 2025) and Bedmachine v4 (Fig. 4c) (Morlighem, 2026).
 339 The Bedmachine v4 also includes 2-30 km scale topography inverted from ice surface observations
 340 (Ockenden et al., 2026). Roughness is generally much higher in our simulated bed compared with
 341 previous interpolations, especially in between radar profiles (Fig. 4a-c). For the Bedmap3 and
 342 Bedmachine v4 grids, respective σ_{2km} domain means are 21 m and 17 m, while domain standard
 343 deviations are 21 m and 16 m. The domain mean σ_{2km} across our results (with ensemble 1σ uncertainty
 344 estimate) is more than double that of previous work at 53 ± 0.2 m, reaching maximums of 390 ± 7 m with
 345 domain standard deviation of 25 ± 0.2 m. Regionally averaged basal roughness is therefore
 346 underestimated by more than 50% in single-interpolation based approaches.

347 The spatial distribution of rougher terrain in the Bedmap3 interpolation is dominated by radar data
 348 availability, as high σ_{2km} is located along survey profiles reaching a maximum of 279 m with little
 349 variability in between. Roughness for the Bedmachine v4 grid is not impacted to the same extent by
 350 measurement availability, although some roughness patterns appear to reflect ice surface features over
 351 the western Belgica Highlands which probably originate from the surface inversion methodology of
 352 Ockenden et al., (2026). Several radar profiles are also still observed in the roughness map (Fig. 4c), likely
 353 due to the inclusion of incompatible ice thickness measurements in the interpolation process. This
 354 emphasises the necessity of our rigorous measurement compatibility analyses and screening steps
 355 before starting interpolation or simulation work. Our simulated beds have improved spatial distribution
 356 of basal roughness which is more consistent with that expected of natural landscapes, with minimal
 357 impacts from measurement distribution on individual bed simulations (Fig. 4a).

358 The pronounced anisotropy in topography in the Dome C region also limits the reliability of ice
 359 thickness or bed surfaces derived using isotropic interpolation strategies, which could mask important
 360 topographic structure by applying uniform smoothing in all directions in data gaps. By explicitly
 361 modelling and incorporating anisotropy into our stochastic simulations we also increase the probability
 362 that realistic structure is simulated in unsurveyed areas. We suggest that future analyses relying on
 363 gridded representations of basal topography such as ice flow and basal conditions modelling should
 364 carefully assess sensitivity to basal roughness before committing to using smoothed interpolations with
 365 unrealistic bed roughness. Our stochastically simulated surfaces preserve natural roughness patterns
 366 and could be used as more realistic boundary conditions for modelling as well as providing a suite of
 367 equally probable inputs for sensitivity analyses to constrain the impacts of bed elevation uncertainties.

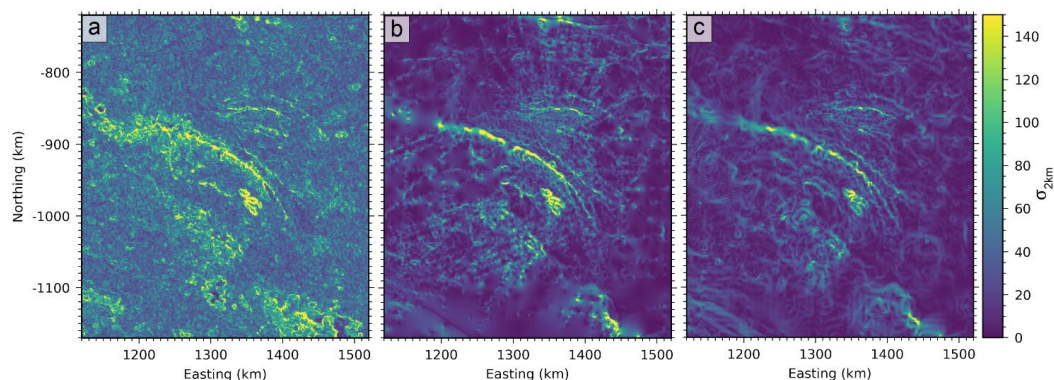


Figure 4: Standard deviation within a 2 km window for gridded ice thickness: **a)** Simulation #001, **b)** Bedmap 3 interpolation, **c)** Bedmachine v4 interpolation.



368 **4.2 Subglacial meltwater drainage**

369 There are 111 locations with radar-inferred subglacial lakes in our simulation domain (Livingstone et
 370 al., 2022), and these occur beneath ice ranging from 2601 m to 4326 m thick. Satellite observations show
 371 that large volumes of meltwater can transit through the subglacial drainage system over short
 372 timescales, with 1.8 km³ of water travelling 290 km over a 16 month period between lakes in the
 373 Adventure Trench (Wingham et al., 2006). We modelled basal hydraulic potential to provide a simplified
 374 assessment of subglacial water flow directions to predict meltwater routing and drainage basins
 375 assuming uniform basal melting. We used the simulated bed ensemble to constrain drainage uncertainty
 376 associated with bed elevation uncertainty and compared this to drainage predictions using the Bedmap
 377 3 interpolation (Fig. 5a,b). Subglacial drainage off the Dome C Plateau is well-constrained, with high
 378 probability for water routing away from the plateau following ice drainage divides and splitting water flow
 379 in either direction of the Concordia Trench (Fig. 5a). Our analyses reveal uncertain drainage divides east
 380 of Concordia Station and towards the western extent of the Belgica Highlands, associated with large
 381 gaps between radar survey profiles.

382 Concordia Lake is the largest subglacial lake within our study area, estimated from radar profiles to
 383 be minimum 45 km long and 16 km wide and containing water volumes of 200 ± 40 km³ (Tikku et al.,
 384 2005). Water inflow to this lake is well-constrained by the Concordia Trench, but outflow and
 385 downstream routing of released meltwater is not well-constrained by radar data. Our simulations
 386 suggest that water could drain either towards Vincennes basin or towards Adventure Trench, and the
 387 most probable drainage basin divides are to the southwest of the lake in contrast to the divides predicted
 388 using Bedmap3 grids (Fig. 5b). The lack of strong basal topographic control over downstream water
 389 routing suggested by limited available radar data indicates that downstream drainage could be sensitive
 390 to migrating ice divides, and more radar surveys are necessary to reduce the uncertainty in water routing.

391

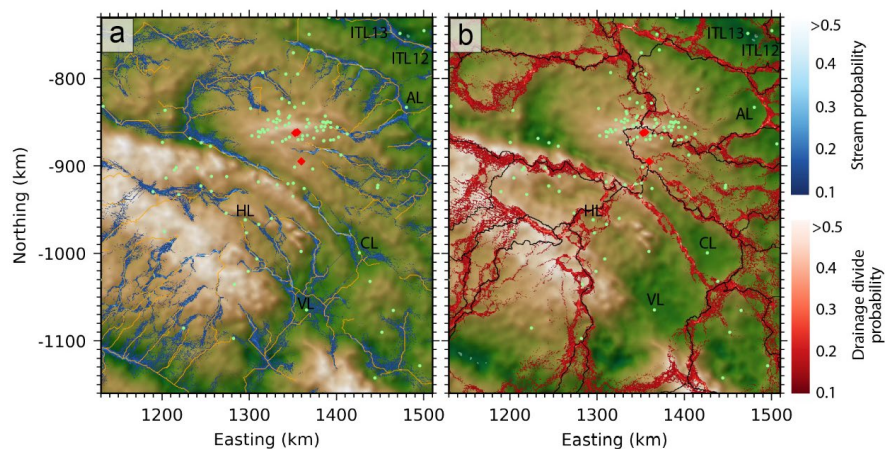


Figure 5: Subglacial drainage predicted using ensemble simulated beds. a) Stream probability calculated from averaged stream predictions over the ensemble (blue), with predicted streams using Bedmap3 bed (orange). b) Drainage divide probability calculated as averaged divides over the ensemble, with divides predicted using Bedmap3 (black). Ice cores also plotted (red diamonds) and radar-detected subglacial lakes (green points). Lakes with estimated minimum surface area >50 km² are labelled: AL = Aurora Lake (Tabacco et al., 2003); CL = Concordia Lake (Oswald and Robin, 1973); HL = Horseshoe Lake (Blankenship et al., 2009); ITL12+13 (Tabacco et al., 2003).

392

393



394 The drainage basin constrained by the western Belgica Highlands and Concordia Ridge contains 11
395 subglacial lakes with a combined radar-estimated surface area of 147 km². Five of these lakes are
396 located beneath thinner ice <3000 m along Concordia Ridge and 6 along the valley floor where ice can be
397 over 3400 m thick. Our stochastic simulations constrain potential flow paths for a drainage system
398 linking these lakes and indicate that large volumes of water draining from this basin could be routed
399 either to the southwest similar to predictions using the Bedmap3 grid or 100 km further north (Fig. 5).

400 The preservation of deep ice layers in undisturbed stratigraphic sequence are sensitive to basal melt,
401 ice flow, and basal ice accretion (Fischer et al., 2013; Van Liefferinge & Pattyn, 2013). Widespread
402 subglacial lakes and meltwater drainage activity evidence basal melting in the Dome C region and poor
403 hydraulic connectivity between lakes could increase potential for basal ice accretion, which together
404 disturb deep ice stratigraphy and limit the preservation of old ice layers. For example, at Lake Concordia
405 enhanced basal melting of 4.3 mm a⁻¹ ± 27% is predicted over most of the lake, and 15.1 m ± 65% of
406 accreted ice in the northeast corner (Thoma et al., 2009). Careful consideration of the subglacial
407 environment is required to identify targets for ice core drill sites and our uncertainty constrained
408 subglacial drainage analyses identify sites with low potential for water ponding or drainage activity (Fig.
409 5a,b).

410

411 **4.3 Geothermal heat flow**

412 The GHF beneath Antarctica is largely unknown, however locally elevated GHF could impact basal
413 conditions and ice flow especially beneath slow-flowing ice dome regions in the absence of frictional
414 heat from basal sliding (Pittard et al., 2016). Ice sheet modelling investigations to identify suitable ice
415 core drilling sites are also sensitive to GHF boundary conditions (Sutter et al., 2019). At Dome C, region-
416 wide means range from 28.6 ± 5.1 to 59.0 ± 3.3 mW m⁻² in large-sale GHF models (An et al., 2015; Burton-
417 Johnson et al., 2020; Hazzard & Richards, 2023; Lösing & Ebbing, 2021; Martos et al., 2017; Purucker,
418 2012; Shen et al., 2020; Stål et al., 2021), and 10's of kilometre scale spatial distributions differ
419 significantly between models (Fig. 6). Local GHF estimates at the EPICA core site of 57.9 ± 6.4 mW m⁻²
420 (Talalay et al., 2020) and 54.5 ± 3.5 (Passalacqua et al., 2017) have high uncertainties and might not
421 reflect regional values. Topographic focussing of geothermal heat lowers the amount of heat received
422 along ridges and increase it in valleys relative to the background value (van der Veen et al., 2007).

423 Using our ensemble of simulated subglacial topography we calculated an adjustment factor to
424 account for local topographic modifications of background GHF following the geostatistical approach of
425 Colgan et al., (2021). We used their equation 2 with empirically determined averaging radius of 5 km and
426 characteristic height needed to induce 100% change in local GHF of 950 m. This calculation was done
427 for each of the simulated beds in our ensemble to produce a topographic adjustment factor map, and
428 Figure 7a shows the ensemble median values. Similar to the ensemble elevation uncertainty,
429 topographic adjustments to GHF are more consistent close to radar profiles, and the map inherently
430 displays lower confidence adjustment factors closer to zero since topographic features far from data
431 vary in location over the ensemble. Locally elevated GHF up to 30% more than the background value can
432 be expected within the troughs (e.g. Adventure, Concordia), yet along ridges (e.g. Concordia) local GHF
433 could be 30% lower (Fig. 7a,b). Beneath the Dome Fuji ice dome, topographic modification to
434 background GHF was predicted to induce widespread local anomalies of ±20%, aggregating to raise the
435 regional average by 0.6% (Shackleton et al., 2023). The Dome C regional mean values are low over the
436 ensemble at 0.05 ± 0.04%, though regional standard deviations 0.1 ± 0.0% indicate widespread potential
437 for localised GHF adjustments of 3-7 mW m⁻² based on modelled range ca. 30-70 mW m⁻².

438

439

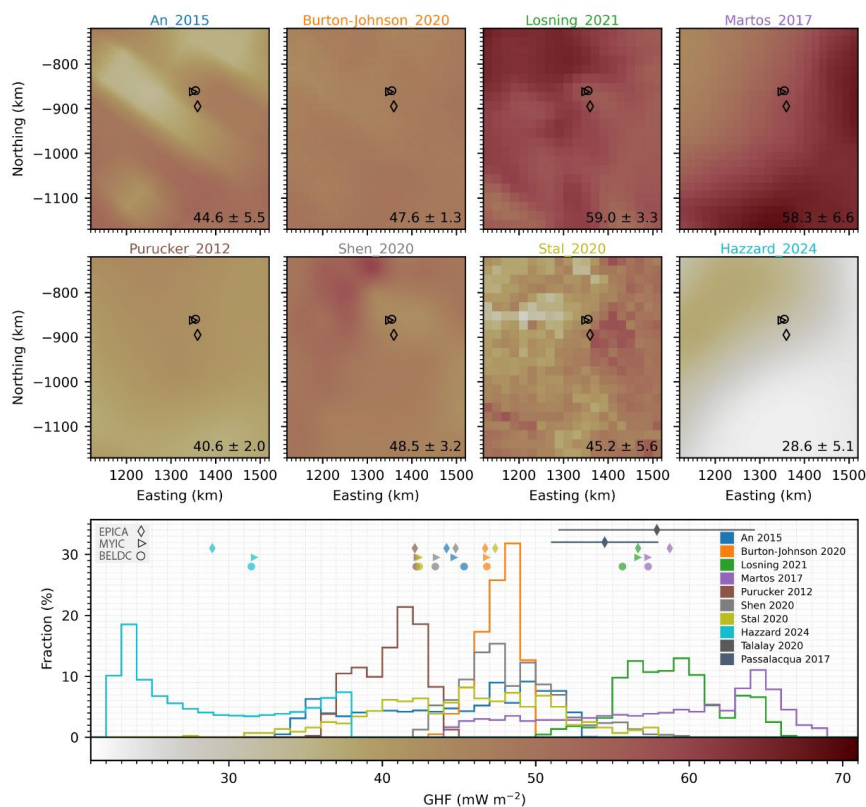


Figure 6: Geothermal heat flow (GHF) estimates near Dome C. Large-scale models plotted as native resolution in the upper 8 maps, with domain mean and standard deviation for each model provided in bottom right corner. Core sites plotted as EPICA: diamond, MYIC: triangle, BELDC: circle. Histograms for modelled GHF are plotted below, with associated value at core sites (diamonds, triangles, circles) together with other local GHF estimates and reported uncertainty at the EPICA core site.

440

441 We find 80% of the radar-inferred subglacial lake sites are within a zone of locally elevated GHF (Fig.
 442 7c), which in conjunction with increased ice thickness could contribute to the spatial pattern of basal
 443 melting and lake distributions. Spatial variability in GHF at much larger scale of 10's of kilometres
 444 increased modelled basal melt rates in the Aurora Basin by up to 4.5% (McCormack et al., 2022).
 445 Smoothed bed in data sparse regions of previous interpolations therefore limits robust assessments of
 446 basal thermal conditions, and using realistically rough topography should be prioritized when delineating
 447 thawed/frozen basal ice and calculating melt rates, which will also improve the reliability of basin-wide
 448 thermodynamical and ice flow modelling. Given the large uncertainties and range of modelled GHF near
 449 Dome C and across Antarctica, the local topographic adjustments to GHF could be used instead to find
 450 suitable sites for future ice coring, prioritising sites with locally lowered GHF. The EPICA core site is
 451 situated in locally elevated GHF by 2% (Fig. 7c), whereas the new sites BELDC and MYIC are situated in a
 452 region with locally lowered GHF by 12 -13% which should be favourable for deep ice layer preservation.
 453 Variability over the ensemble is less than 0.08% for all ice core sites since they are generally close to
 454 radar data. Borehole GHF estimates should also be adjusted to account for local topographic
 455 modifications before extrapolating over a larger region.

456

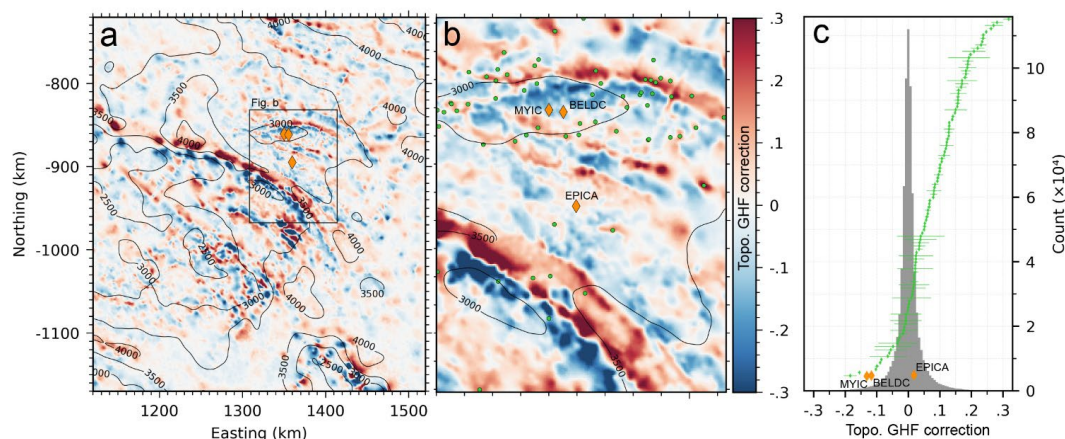


Figure 7: Topographic adjustments to geothermal heat flow (GHF). **a)** Local topographic adjustments to GHF displayed as the median adjustments over the ensemble of 100 simulated bed elevation grids. Ice thickness contours at 500 m intervals are drawn in black. **b)** Enlarged view of the central plateau near the ice core sites, also with radar-inferred subglacial lakes drawn as green points. **c)** Histogram of topographic adjustments, with ensemble median sampled adjustments at the subglacial lake sites (green) and core sites (orange) with median absolute deviation error bar.

457

458

5. Conclusions

459

460

461

462

463

464

465

466

467

468

469

470

471

472

473

474

475

476

477

478

479

480

481

482

483

484

485

New airborne radar surveys uncover previously unmapped sectors of the Belgica Highlands, and we used a rigorous approach to integrating new observations with available ice thickness data near Dome C. Our measurement compatibility analysis guided strict filtering procedures, and we find that rigorous quality screening and cross-validation to integrate new measurements with existing data is crucial for characterising basal roughness. This process is a necessary pre-requisite for reliable gridding or simulating of bed topography to minimize the impact that nearby inconsistent measurements have on spatial statistics. Our simulated bed has improved representation of basal roughness in data sparse regions, with region-wide means more than double those of previous work and spatial patterns free from the influence of radar survey geometry. The ensemble simulation approach for mapping elevation uncertainty accounts for the combined influence of data density and local bed roughness characteristics, producing higher uncertainties where measurements are sparse and the terrain is rough. Domain-mean bed elevation uncertainty is 53 m and reaches 260 m in data-sparse regions, however, near the BELDC and MYIC ice core sites dense radar coverage constrains elevation uncertainty effectively to zero at a 500 m grid scale.

Subglacial drainage analyses using ensemble simulated bed identify well-constrained drainage away from the Dome C Plateau, but poorly constrained outflow from Concordia Lake and western Belgica Highlands drainage basin. These uncertainties impact predictions of subglacial lake connectivity and downstream water transport, highlighting locations where additional radar surveys are required to adequately constrain subglacial drainage. Our work also reveals the pattern of local topographic modifications to regional GHF, which could be critical to delineating thawed/frozen bed, locating suitable sites for ice core drilling, and interpreting retrieved cores and borehole measurements/modelling investigations. We identify locations where local bed topography could lower GHF by up to 30% of the regional value, and the MYIC and BELDC ice core drilling sites are within a zone of locally lowered GHF by 12% which should be favourable for preserving deep ice layer continuity. Topographic focussing of geothermal heat likely enhances basal melting in many trough locations and could exert a control over the distribution of subglacial lakes, with most radar-inferred subglacial lakes occurring in a region of locally elevated GHF. Given the large spread among continental-scale GHF models, we suggest that



486 locally resolved topographic adjustments to GHF provide an independent and complementary constraint
487 on spatial variability in basal conditions.

488 Our study emphasizes that the physical realism of Antarctic subglacial boundary conditions
489 depends on capturing the inherent variability and anisotropy of the bed. These properties are currently
490 obscured in widely used Antarctic bed products due to smoothing from isotropic deterministic
491 interpolation, which limits their reliability for use in ice-sheet and subglacial environment modelling.
492 Survey design should capture directional anisotropy by acquiring profiles along multiple azimuths,
493 extending beyond traditional along- and across-flow transects, while gridded products should prioritize
494 simulation-based approaches that maintain realistic spatial continuity in data-sparse regions. By
495 resolving variability at scales relevant to basal processes and adopting ensemble-based topography, the
496 community can more effectively propagate measurement and interpolation uncertainties into
497 subsequent ice-sheet and subglacial environment analyses.

498 6. Acknowledgements

499 This research was supported by funding from Korea Institute of Marine Science & Technology
500 Promotion (KIMST) grant funded by the Ministry of Oceans and Fisheries (KIMST RS-2026-25521468), and
501 Research Council of Norway (FRINATEK 315246). The Technical University of Denmark acquired POLARIS
502 data under ESA Contract No. 4000144378/23/NL/CT, supported by the European Space Agency (ESA),
503 Australian Antarctic Division, and Institut Polaire Français Paul Émile Victor. Computing resources from
504 Sigma2 – the National Infrastructure for High-Performance Computing and Data Storage in Norway were
505 utilised in this work through project NN10061K. We also acknowledge the many researchers,
506 institutions, and national Antarctic programmes who have contributed ice thickness data to the Bedmap
507 Database and appreciate the community commitment to open data and software sharing which is
508 essential for advancing Antarctic science. The Norwegian Polar Institute contribution forms part of the
509 EU Horizon 2020 Beyond EPICA Oldest Ice Core (BE-OIC) project (Grant 815384). This is BE-OI
510 contribution number XX.

511 Code availability

512 Code used for geostatistical modelling and stochastic simulation is available at:
513 <https://github.com/calvinshackleton/DomeC-BedElevation.git> (Shackleton, 2026), which are based on
514 tools from open-source python software: Verde (Uieda, 2018), GeoStatsPy (Pyrzcz et al., 2021), SciKit
515 Gstat (Mälicke et al., 2021), GStatSim (MacKie et al., 2023).

516 Data availability

517 Appendix animation A, as well as ensemble grids of simulated ice thickness, bed elevation, and local
518 topographic adjustments to geothermal heat flow are available as GeoTIFFs from the Norwegian Polar
519 Data Centre via: <https://doi.org/10.21334/NPOLAR.2026.D05BFE78> (Shackleton and Matsuoka, 2026).

520 Author contributions

521 CS and KM conceptualized the study, developed the methodology, and wrote the manuscript. CS
522 carried out the analysis, wrote the workflow code, and performed the simulations. BF, JL, AR, PG, DT, HTJ,
523 CC, and CS contributed to the collection and processing of the KOPRI/UA radar data. JD and AK
524 contributed to the collection and processing of the DTU radar data. All authors contributed to the
525 preparation of the final manuscript.



526 **Competing interests**

527 The contact author declares that none of the authors have any competing interests.

528

529 **References**

- 530 An, M., Wiens, D. A., Zhao, Y., Feng, M., Nyblade, A., Kanao, M., et al. (2015). Temperature, lithosphere-
531 asthenosphere boundary, and heat flux beneath the Antarctic Plate inferred from seismic
532 velocities. *Journal of Geophysical Research: Solid Earth*, 120(12), 8720–8742.
533 <https://doi.org/10.1002/2015JB011917>
- 534 Arthur, J. F., Shackleton, C., Moholdt, G., Matsuoka, K., & van Oostveen, J. (2025). Evidence of active
535 subglacial lakes under a slowly moving coastal region of the Antarctic Ice Sheet. *The Cryosphere*,
536 19(1), 375–392. <https://doi.org/10.5194/tc-19-375-2025>
- 537 Awasthi, A., D. Taylor, S. Kolpuke, O. Reyhanigalangashi, L. Vanderburgh, D. Elluru, C. O'Neill, C. Chung,
538 J. Lee and S. Gogineni, "High-sensitivity transceiver for airborne ultra-wideband radio echo
539 sounding of polar regions," in *2022 IEEE Microwaves, Antennas, and Propagation Conference*
540 *(MAPCON)*, Bangalore, India, 2022.
- 541 Bartos, M. (2020). pysheds. Python. 10.5281/zenodo.3822494
- 542 Berends, C. J., Köhler, P., Lourens, L. J., & van de Wal, R. S. W. (2021). On the Cause of the Mid-
543 Pleistocene Transition. *Reviews of Geophysics*, 59(2), e2020RG000727.
544 <https://doi.org/10.1029/2020RG000727>
- 545 Blankenship, D. D., Kempf, S. D., Young, D. A., Richter, T. G., Schroeder, D. M., Greenbaum, J. S., Holt, J.
546 W., van Ommen, T., Warner, R. C., Roberts, J. L., Young, N. W., Lemeur, E. & Siegert, M. J. (2011).
547 IceBridge HiCARS 1 L2 Geolocated Ice Thickness. (IR1HI2, Version 1). [Data Set]. Boulder,
548 Colorado USA. NASA National Snow and Ice Data Center Distributed Active Archive Center.
549 <https://doi.org/10.5067/F5FGUT9F5089>.
- 550 Blankenship, D. D., Kempf, S. D., Young, D. A., Richter, T. G., Schroeder, D. M., Greenbaum, J. S., van
551 Ommen, T., Warner, R. C., Roberts, J. L., Young, N. W., Lemeur, E., Siegert, M. J. & Holt, J. W.
552 (2017). IceBridge HiCARS 1 L1B Time-Tagged Echo Strength Profiles. (IR1HI1B, Version 1). [Data
553 Set]. Boulder, Colorado USA. NASA National Snow and Ice Data Center Distributed Active Archive
554 Center. <https://doi.org/10.5067/W2KXX0MYNJ9G>.
- 555 Blankenship, D. D., Kempf, S. D., & Young, D. A. (2022) "Support Office for Airborne Research 1 km
556 sampled ice thickness data" U.S. Antarctic Program (USAP) Data Center. doi:
557 <https://doi.org/10.15784/601588>.
- 558 Bianchi, C.; Cafarella, L.; De Michelis, P.; Forieri, A.; Frezzotti, M.; Tabacco, I. E.; Zirizzotti, A. Radio Echo
559 Sounding (RES) Investigations at Talos Dome (East Antarctica): Bedrock Topography and Ice
560 Thickness. *Ann. Geophys.* (2009), 46 (6). <https://doi.org/10.4401/ag-3471>.
- 561 Burton-Johnson, A., Dziadek, R., & Martin, C. (2020). Review article: Geothermal heat flow in Antarctica:
562 current and future directions. *The Cryosphere*, 14(11), 3843–3873. <https://doi.org/10.5194/tc-14-3843-2020>
- 564 Chung, A., Parrenin, F., Steinhage, D., Mulvaney, R., Martín, C., Cavitte, M. G. P., et al. (2023a). Internal
565 reflecting horizons at Little Dome C, Antarctica [Application/zip]. PANGAEA.
566 <https://doi.org/10.1594/PANGAEA.957176>



- 567 Chung, A., Parrenin, F., Steinhage, D., Mulvaney, R., Martín, C., Cavitte, M. G. P., et al. (2023b). Stagnant
568 ice and age modelling in the Dome C region, Antarctica. *The Cryosphere*, 17(8), 3461–3483.
569 <https://doi.org/10.5194/tc-17-3461-2023>
- 570 Chung, Ailsa; Parrenin, Frédéric; Steinhage, Daniel; Mulvaney, Rob; Martín, Carlos; Cavitte, Marie G
571 P; Lilien, David A; Helm, Veit; Taylor, Drew; Gogineni, Prasad; Ritz, Catherine; Frezzotti,
572 Massimo; O'Neill, Charles; Miller, Heinrich; Dahl-Jensen, Dorthe; Eisen, Olaf (2023c): Bedrock at
573 Little Dome C, Antarctica [dataset]. *PANGAEA*, <https://doi.org/10.1594/PANGAEA.957461>
- 574 Cianfarra, P., Forieri, A., Salvini, F., Tabacco, I. E., & Zirizzotti, A. (2009). Geological setting of the
575 Concordia Trench-Lake system in East Antarctica. *Geophysical Journal International*, 177(3),
576 1305–1314. <https://doi.org/10.1111/j.1365-246X.2009.04123.x>
- 577 Colgan, W., MacGregor, J. A., Mankoff, K. D., Haagenson, R., Rajaram, H., Martos, Y. M., et al. (2021).
578 Topographic Correction of Geothermal Heat Flux in Greenland and Antarctica. *Journal of*
579 *Geophysical Research: Earth Surface*, 126(2). <https://doi.org/10.1029/2020JF005598>
- 580 Cuffey, K. M., & Paterson, W. S. B. (2010). *The Physics of Glaciers* (4th ed.). Elsevier.
- 581 Dall, J., Kristensen, S. S., Krozer, V., Hernández, C. C., Vidkjær, J., Kusk, A., et al. (2010). ESA'S
582 POLarimetric Airborne Radar Ice Sounder (POLARIS): design and first results. *IET Radar, Sonar &*
583 *Navigation*, 4(3), 488–496. <https://doi.org/10.1049/iet-rsn.2009.0035>
- 584 Dall, J., U. Nielsen, A. Kusk, R.S.W. van de Wal, “Ice flow mapping with P-band SAR”, *Proceedings of the*
585 *IEEE 2013 International Geoscience and Remote Sensing Symposium*, 4 p., Melbourne, July
586 2013.
- 587 Deutsch, C. V., & Journel, A. G. (1997). *GSLIB: Geostatistical software library and user guide* (Second
588 Edition). New York: Oxford University Press. [http://claytonvdeutsch.com/wp-](http://claytonvdeutsch.com/wp-content/uploads/2019/03/GSLIB-Book-Second-Edition)
589 [content/uploads/2019/03/GSLIB-Book-Second-Edition](http://claytonvdeutsch.com/wp-content/uploads/2019/03/GSLIB-Book-Second-Edition)
- 590 Drewry, D. J., Jordan, S. R., & Jankowski, E. (1982). Measured Properties of the Antarctic Ice Sheet:
591 Surface Configuration, Ice Thickness, Volume and Bedrock Characteristics. *Annals of Glaciology*,
592 3, 83–91. <https://doi.org/10.3189/S0260305500002573>
- 593 Ferraccioli, F., Corr, H., Jordan, T., Robinson, C., Armadillo, E., & Armadillo, G. (2018). Airborne radar bed
594 elevation picks across the Wilkes Subglacial Basin, 2005–2006 [Data set]. Polar Data Centre,
595 Natural Environment Research Council, UK. [https://doi.org/10.5285/59e5a6f5-e67d-4a05-99af-](https://doi.org/10.5285/59e5a6f5-e67d-4a05-99af-30f65656940)
596 [30f65656940](https://doi.org/10.5285/59e5a6f5-e67d-4a05-99af-30f65656940)
- 597 Fischer, H., Severinghaus, J., Brook, E., Wolff, E., Albert, M., Alemany, O., et al. (2013). Where to find 1.5
598 million yr old ice for the IPICS “Oldest-Ice” ice core. *Climate of the Past*, 9(6), 2489–2505.
599 <https://doi.org/10.5194/cp-9-2489-2013>
- 600 Forieri, A., Zucconi, L., Bini, A., Zirizzotti, A., Remy, F., & Tabacco, I. E. (2004). New bedrock map of Dome
601 C, Antarctica, and morphostructural interpretation of the area. *Annals of Glaciology*, 39, 321–
602 325. <https://doi.org/10.3189/172756404781814456>
- 603 Frezzotti M, Bitelli G, De Michelis P, et al. Geophysical survey at Talos Dome, East Antarctica: the search
604 for a new deep-drilling site. *Annals of Glaciology*. (2004) 39:423-432.
605 <https://doi.org/10.3189/1727564047818144591>
- 606 Frémand, A. C., Fretwell, P., Bodart, J. A., Pritchard, H. D., Aitken, A., Bamber, J. L., et al. (2023). Antarctic
607 Bedmap data: Findable, Accessible, Interoperable, and Reusable (FAIR) sharing of 60 years of ice
608 bed, surface, and thickness data. *Earth System Science Data*, 15(7), 2695–2710.
609 <https://doi.org/10.5194/essd-15-2695-2023>



- 610 Hazzard, J. A. N., & Richards, F. D. (2023). Antarctic Geothermal Heat Flow, Crustal Conductivity and
611 Heat Production Inferred From Seismological Data. Retrieved from
612 <https://eartharxiv.org/repository/view/5939/>
- 613 Howat, I. M., Porter, C., Smith, B. E., Noh, M.-J., & Morin, P. (2019). The Reference Elevation Model of
614 Antarctica. *The Cryosphere*, 13(2), 665–674. <https://doi.org/10.5194/tc-13-665-2019>
- 615 Jouzel, J., Masson-Delmotte, V., Cattani, O., Dreyfus, G., Falourd, S., Hoffmann, G., et al. (2007). Orbital
616 and Millennial Antarctic Climate Variability over the Past 800,000 Years. *Science*, 317(5839), 793–
617 796. <https://doi.org/10.1126/science.1141038>
- 618 Kusk, A., J. Dall, “SAR focusing of P-band ice sounding data using back-projection”, *Proceedings of the*
619 *IEEE 2010 International Geoscience and Remote Sensing Symposium*, pp. 4071-4074, Honolulu,
620 July 2010.
- 621 Law, R., Christoffersen, P., MacKie, E., Cook, S., Haseloff, M., & Gagliardini, O. (2023). Complex motion of
622 Greenland Ice Sheet outlet glaciers with basal temperate ice. *Science Advances*, 9(6), eabq5180.
623 <https://doi.org/10.1126/sciadv.abq5180>
- 624 Lee, J. S., Jurkevich, L., Dewaele, P., Wambacq, P., & Oosterlinck, A. (1994). Speckle filtering of synthetic
625 aperture radar images: A review. *Remote Sensing Reviews*, 8(4), 313–340.
626 <https://doi.org/10.1080/02757259409532206>
- 627 Lisiecki, L. E., & Raymo, M. E. (2005). A Pliocene–Pleistocene stack of 57 globally distributed benthic δ
628 ^{18}O records. *Paleoceanography*, 20(1), 1–17. <https://doi.org/10.1029/2004PA001071>
- 629 Livingstone, S. J., Li, Y., Rutishauser, A., Sanderson, R. J., Winter, K., Mikucki, J. A., et al. (2022). Subglacial
630 lakes and their changing role in a warming climate. *Nature Reviews Earth & Environment*, 1–19.
631 <https://doi.org/10.1038/s43017-021-00246-9>
- 632 Lösing, M., & Ebbing, J. (2021). Predicting Geothermal Heat Flow in Antarctica With a Machine Learning
633 Approach. *Journal of Geophysical Research: Solid Earth*, 126(6), e2020JB021499.
634 <https://doi.org/10.1029/2020JB021499>
- 635 Lüthi, D., Le Floch, M., Bereiter, B., Blunier, T., Barnola, J.-M., Siegenthaler, U., et al. (2008). High-
636 resolution carbon dioxide concentration record 650,000–800,000 years before present. *Nature*,
637 453(7193), 379–382. <https://doi.org/10.1038/nature06949>
- 638 MacKie, E. J., Schroeder, D. M., Caers, J., Siegfried, M. R., & Scheidt, C. (2020). Antarctic Topographic
639 Realizations and Geostatistical Modeling Used to Map Subglacial Lakes. *Journal of Geophysical*
640 *Research: Earth Surface*, 125(3), e2019JF005420. <https://doi.org/10.1029/2019JF005420>
- 641 MacKie, Emma J., Schroeder, D. M., Zuo, C., Yin, Z., & Caers, J. (2021). Stochastic modeling of subglacial
642 topography exposes uncertainty in water routing at Jakobshavn Glacier. *Journal of Glaciology*,
643 67(261), 75–83. <https://doi.org/10.1017/jog.2020.84>
- 644 MacKie, Emma J., Field, M., Wang, L., Yin, Z., Schoedl, N., Hibbs, M., & Zhang, A. (2023). GStatSim V1.0: a
645 Python package for geostatistical interpolation and conditional simulation. *Geoscientific Model*
646 *Development*, 16(13), 3765–3783. <https://doi.org/10.5194/gmd-16-3765-2023>
- 647 MacGregor, J. A., Boisvert, L. N., Medley, B., Petty, A. A., Harbeck, J. P., Bell, R. E., et al. (2021). The
648 scientific legacy of NASA’s Operation IceBridge. *Reviews of Geophysics*, 59, e2020RG000712.
649 <https://doi.org/10.1029/2020RG000712>
- 650 Mälicke, M., Möller, E., Schneider, H. D., & Müller, S. (2021, May 28). mmaelicke/scikit-gstat: A scipy
651 flavoured geostatistical variogram analysis toolbox. Zenodo.
652 <https://doi.org/10.5281/zenodo.4835779>



- 653 Martos, Y. M., Catalán, M., Jordan, T. A., Golynsky, A., Golynsky, D., Eagles, G., & Vaughan, D. G. (2017).
654 Heat Flux Distribution of Antarctica Unveiled. *Geophysical Research Letters*, 44(22), 11,417-
655 11,426. <https://doi.org/10.1002/2017GL075609>
- 656 McCormack, F. S., Roberts, J. L., Dow, C. F., Stål, T., Halpin, J. A., Reading, A. M., & Siegert, M. J. (2022).
657 Fine-Scale Geothermal Heat Flow in Antarctica Can Increase Simulated Subglacial Melt
658 Estimates. *Geophysical Research Letters*, 49(15), e2022GL098539.
659 <https://doi.org/10.1029/2022GL098539>
- 660 Morlighem, M. (2026). MEaSURES BedMachine Antarctica, Version 4 [Data set]. NASA National Snow and
661 Ice Data Center Distributed Active Archive Center. <https://doi.org/10.5067/POJQI54A45HX>
- 662 Mulvaney, R., Frezzotti, M., Ritz, C., Martín, C., Rix, J., & Chung, A. (2023). Bedrock in the Dome C region
663 of Antarctica [Text/tab-separated-values]. PANGAEA. <https://doi.org/10.1594/PANGAEA.963474>
- 664 Nielsen, U., J. Dall, "Direction-of-Arrival estimation for radar ice sounding surface clutter suppression",
665 *IEEE Transactions on Geoscience and Remote Sensing*, Vol. 53, No. 9, pp. 5170-5179, September
666 2015.
- 667 Ockenden, H., Bingham, R. G., Goldberg, D., Curtis, A., & Morlighem, M. (2026). Complex mesoscale
668 landscapes beneath Antarctica mapped from space. *Science*, 391(6782), 314–319.
669 <https://doi.org/10.1126/science.ady2532>
- 670 Parrenin, F., Cavitte, M. G. P., Blankenship, D. D., Chappellaz, J., Fischer, H., Gagliardini, O., et al. (2017).
671 Is there 1.5-million-year-old ice near Dome C, Antarctica? *Cryosphere*, 11(6), 2427–2437.
672 <https://doi.org/10.5194/tc-11-2427-2017>
- 673 Passalacqua, O., Ritz, C., Parrenin, F., Urbini, S., & Frezzotti, M. (2017). Geothermal flux and basal melt
674 rate in the Dome C region inferred from radar reflectivity and heat modelling. *Cryosphere*, 11(5),
675 2231–2246. <https://doi.org/10.5194/tc-11-2231-2017>
- 676 Pittard, M. L., Galton-Fenzi, B. K., Roberts, J. L., & Watson, C. S. (2016). Organization of ice flow by
677 localized regions of elevated geothermal heat flux. *Geophysical Research Letters*, 43(7), 3342–
678 3350. <https://doi.org/10.1002/2016GL068436>
- 679 Pritchard, H. D., Fretwell, P. T., Fremand, A. C., Bodart, J. A., Kirkham, J. D., Aitken, A., et al. (2025).
680 Bedmap3 updated ice bed, surface and thickness gridded datasets for Antarctica. *Scientific
681 Data*, 12(1), 414. <https://doi.org/10.1038/s41597-025-04672-y>
- 682 Purucker, M. (2012). Geothermal heat flux data set based on low resolution observations collected by the
683 CHAMP satellite between 2000 and 2010, and produced from the MF-6 model following the
684 technique described in Fox Maule et al., (2005). Retrieved June 9, 2022, from
685 http://webserv.cs.umn.edu/isis/index.php/Main_Page
- 686 Pycrz, M., Jo, H., Kuppenko, A., Liu, W., Gigliotti, A. E., Salomaki, T., & Javier, S. (2021, October).
687 GeostatsPy: Geostatistical Library in Python (Version 1.0.0). <https://doi.org/10.5281/zenodo>.
- 688 Rizvi, S., M. Thapa, B. Fraysher, A. Rapadas, S. Neshani, D. Taylor, J. Lee, D. Dahl-Jensen, S. Gogineni, S.
689 Kolpuke and C. Chung, "Fine-Resolution Mapping of Near-Bed Ice Layers with Ultra-Wideband
690 Radars," in *AGU 2025*, New Orleans, LA, USA, 2025.
- 691 Shackleton, C., Matsuoka, K., Moholdt, G., Van Liefferinge, B., & Paden, J. (2023). Stochastic Simulations
692 of Bed Topography Constrain Geothermal Heat Flow and Subglacial Drainage Near Dome Fuji,
693 East Antarctica. *Journal of Geophysical Research: Earth Surface*, 128(11), e2023JF007269.
694 <https://doi.org/10.1029/2023JF007269>



- 695 Shackleton, C. (2026). DomeC-BedElevation [software]. <https://github.com/calvinshackleton/DomeC->
696 [BedElevation.git](https://github.com/calvinshackleton/DomeC-BedElevation.git)
- 697 Shackleton, C., & Matsuoka, K. (2026). Simulated ice thickness, bed elevation and local topographic
698 adjustments to geothermal heat flow near Dome C, Antarctica [Dataset]. Norwegian Polar
699 Institute. <https://doi.org/10.21334/NPOLAR.2026.D05BFE78>
- 700 Shen, W., Wiens, D. A., Lloyd, A. J., & Nyblade, A. A. (2020). A Geothermal Heat Flux Map of Antarctica
701 Empirically Constrained by Seismic Structure. *Geophysical Research Letters*, 47(14),
702 e2020GL086955. <https://doi.org/10.1029/2020GL086955>
- 703 Shreve, R. L. (1972). The movement of water in glaciers. *Journal of Glaciology*, 11(62), 205–214.
- 704 Skolnik, M. I. (2008). *Radar handbook* (3rd ed). New York: McGraw-Hill.
- 705 Steinhage, Daniel; Franke, Steven; Eisen, Olaf; Miller, Heinrich; Helm, Veit (2023): Ice Thickness from
706 East Antarctica, over Dome C, Dome A, Talos Dome and Vostok recorded with the airborne AWI
707 EMR radar system in 2007/2008 [dataset]. PANGAEA, <https://doi.org/10.1594/PANGAEA.957066>
- 708 Stål, T., Reading, A. M., Halpin, J. A., & Whittaker, J. M. (2021). Antarctic Geothermal Heat Flow Model:
709 Aq1. *Geochemistry, Geophysics, Geosystems*, 22(2), e2020GC009428.
710 <https://doi.org/10.1029/2020GC009428>
- 711 Stolt, R. H. (1978). Migration by Fourier transform. *Geophysics*, 43(1), 23–48.
712 <https://doi.org/10.1190/1.1440826>
- 713 Sutter, J., Fischer, H., Grosfeld, K., Karlsson, N. B., Kleiner, T., Van Liefferinge, B., & Eisen, O. (2019).
714 Modelling the Antarctic Ice Sheet across the mid-Pleistocene transition – implications for Oldest
715 Ice. *The Cryosphere*, 13(7), 2023–2041. <https://doi.org/10.5194/tc-13-2023-2019>
- 716 Tabacco, I. E., Passerini, A., Corbelli, F., & Gorman, M. (1998). Determination of the surface and bed
717 topography at Dome C, East Antarctica. *Journal of Glaciology*, 44(146), 185–191.
718 <https://doi.org/10.3189/S0022143000002501>
- 719 Taylor, J., Siegert, M. J., Payne, A. J., & Hubbard, B. (2004). Regional-scale bed roughness beneath ice
720 masses: measurement and analysis. *Computers & Geosciences*, 30(8), 899–908.
721 <https://doi.org/10.1016/j.cageo.2004.06.007>
- 722 Thoma, M., Grosfeld, K., Filina, I., & Mayer, C. (2009). Modelling flow and accreted ice in subglacial Lake
723 Concordia, Antarctica. *Earth and Planetary Science Letters*, 286(1), 278–284.
724 <https://doi.org/10.1016/j.epsl.2009.06.037>
- 725 Tikku, A. A., Bell, R. E., Studinger, M., Clarke, G. K. C., Tabacco, I., & Ferraccioli, F. (2005). Influx of
726 meltwater to subglacial Lake Concordia, East Antarctica. *Journal of Glaciology*, 51(172), 96–104.
727 <https://doi.org/10.3189/172756505781829494>
- 728 Uieda, L. (2018). Verde: Processing and gridding spatial data using Green's functions. *Journal of Open*
729 *Source Software*, 3(30), 957. <https://doi.org/10.21105/joss.00957>
- 730 Van Liefferinge, B., & Pattyn, F. (2013). Using ice-flow models to evaluate potential sites of million year-
731 old ice in Antarctica. *Climate of the Past*, 9, 2335–2345.
- 732 Van Liefferinge, B., Pattyn, F., Cavitte, M. G. P., Karlsson, N. B., Young, D. A., Sutter, J., & Eisen, O. (2018).
733 Promising oldest ice sites in east antarctica based on thermodynamical modelling. *Cryosphere*,
734 12(8), 2773–2787. <https://doi.org/10.5194/tc-12-2773-2018>



- 735 van der Veen, C. J., Leftwich, T., von Frese, R., Csatho, B. M., & Li, J. (2007). Subglacial topography and
736 geothermal heat flux: Potential interactions with drainage of the Greenland ice sheet.
737 *Geophysical Research Letters*, 34(12). <https://doi.org/10.1029/2007GL030046>
- 738 Wang, Z., Chung, A., Steinhage, D., Parrenin, F., Freitag, J., & Eisen, O. (2023). Mapping age and basal
739 conditions of ice in the Dome Fuji region, Antarctica, by combining radar internal layer
740 stratigraphy and flow modeling. *The Cryosphere Discussions*, 1–22. [https://doi.org/10.5194/tc-](https://doi.org/10.5194/tc-2023-35)
741 [2023-35](https://doi.org/10.5194/tc-2023-35)
- 742 Wingham, D. J., Siegert, M. J., Shepherd, A., & Muir, A. S. (2006). Rapid discharge connects Antarctic
743 subglacial lakes. *Nature*, 440(7087), 1033–1036. <https://doi.org/10.1038/nature04660>
- 744 Winter, A., Steinhage, D., Creyts, T. T., Kleiner, T., and Eisen, O.: Age stratigraphy in the East Antarctic Ice
745 Sheet inferred from radio-echo sounding horizons, *Earth Syst. Sci. Data*, (2019) 11, 1069–1081,
746 <https://doi.org/10.5194/essd-11-1069-2019>
- 747 Young, D. A., Roberts, J. L., Ritz, C., Frezzotti, M., Quartini, E., Cavitte, M. G. P., et al. (2017). High-
748 resolution boundary conditions of an old ice target near Dome C, Antarctica. *The Cryosphere*,
749 11(4), 1897–1911. <https://doi.org/10.5194/tc-11-1897-2017>
- 750 Young, D. A., Beem, L. H., Blankenship, D. D., Cavitte, M., Greenbaum, J., Habbal, F., et al. (2020)
751 "ICECAP: High resolution survey of the Little Dome C region in support of the IPICS Old Ice goal"
752 U.S. Antarctic Program (USAP) Data Center. doi: <https://doi.org/10.15784/601355>.
- 753 Xiangbin, C., Jeofry, H., Greenbaum, J., Roberts, J., Blankenship, D., Bo, S., & Siegert, M. (2020). ICECAP-2
754 consortium processed airborne ice thickness data from the Princess Elizabeth Land, East
755 Antarctica [Data set]. Zenodo. <https://doi.org/10.5281/zenodo.4023393>
- 756
- 757
- 758
- 759
- 760
- 761
- 762
- 763
- 764
- 765
- 766
- 767
- 768
- 769
- 770
- 771



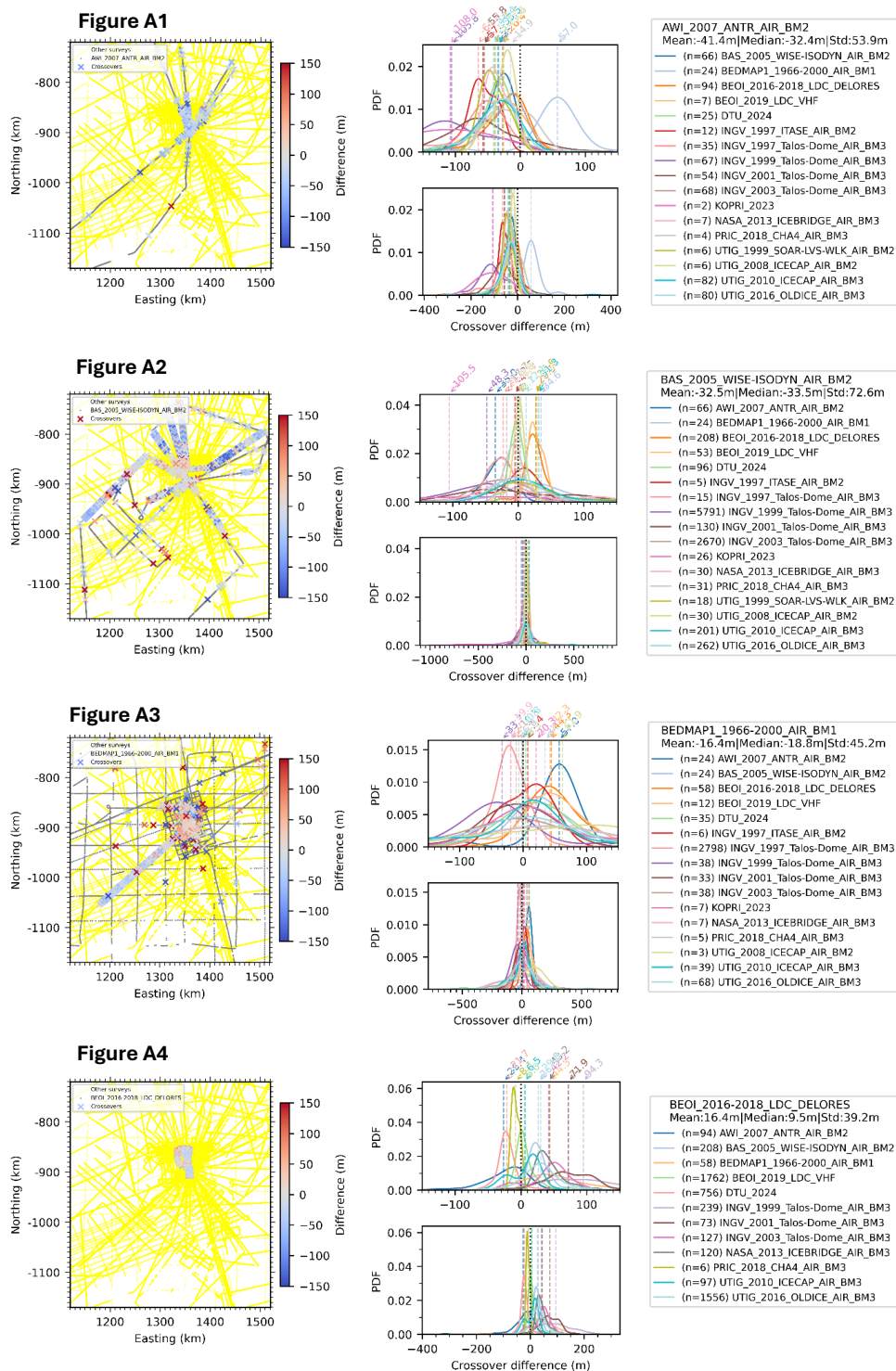
Appendix A

Table A1: Radar-derived ice thickness datasets used. BAS = British Antarctic Survey, BE-OI = Beyond EPICA Oldest Ice, KOPRI = Korean Polar Research Institute, UA = University of Alabama, DTU = The Technical University of Denmark, CPH = University of Copenhagen, AWI = Alfred Wegener Institute, AAD = Australian Antarctic Division, INGV = Istituto Nazionale di Geofisica e Vulcanologia, UTIG = University of Texas Institute for Geophysics, NASA = National Aeronautics and Space Administration, PRIC = Polar Research Institute of China, LDEO = Lamont-Doherty Earth Observatory, CRISIS = Center for Remote Sensing of Ice Sheets. *All surveys had data filtered out within 0.6 km of crossover sites if differences were > 50 m, with priority determined by mean absolute differences between all other surveys.

#	Name	Institution	Survey/Project	System	Source/DOI/Key reference	Filtering Notes*
1	AWI_2007_ANTR_AIR_BM2	AWI	Dronning Maud Land; Princess Elizabeth Land; Dome A; Dome C	AWI EMR	https://doi.org/10.1594/PANGAEA.957066 https://doi.org/10.5194/essd-11-10695-2019	
2	BAS_2005_WISE-ISODYN_AIR_BM2	BAS	Wilkes Subglacial Basin (WISE-ISODYN)	PASIN	https://doi.org/10.5285/595a56f6-467d-4d05-9961-30f656569401 https://doi.org/10.5194/essd-14-3379-2022	Filtered out data within 0.2 km of surveys #9 and #11 due to inconsistencies.
3	BEDMAP1_1966-2000_AIR_BM1	Various	Various	Various	https://doi.org/10.5194/essd-15-2695-2023	Filtered out data along 5 manually supplied lines due to inconsistencies with surrounding data. Also filtered out data within 10 km of more recent data.
4	BE-OI_2016-2018_LDC_DELORES	BAS	BE-OI	DELORES	https://doi.org/10.1594/PANGAEA.963474	Filtered out data along 1 manually supplied line due to inconsistencies with surrounding data.
5	BE-OI_2019_LDC_VHF	UA/CPH/AWI	BE-OI	VHF	https://doi.org/10.1594/PANGAEA.957461	
6	DTU_2024	DTU	ICESAR2024 & ICECAP	POLARIS	https://zenodo.org/records/4897049	
7	INGV_1997_ITASE_AIR_BM2	INGV	Talos Dome; Oats Land (ITASE)	INGV-IT GlacioRadar	https://doi.org/10.3189/17275600781814691 1	Filtered out data within 0.2 km of surveys #8, #9, #10 due to duplicated data.
8	INGV_1997_Talos-Dome_AIR_BM3	INGV	Talos Dome; Terre Adelie	INGV-IT GlacioRadar	https://doi.org/10.4401/ig-3471	
9	INGV_1999_Talos-Dome_AIR_BM3	INGV	Talos Dome; Terre Adelie	INGV-IT GlacioRadar	https://doi.org/10.4401/ig-3471	
10	INGV_2001_Talos-Dome_AIR_BM3	INGV	Talos Dome; Oats Land	INGV-IT GlacioRadar	https://doi.org/10.5194/essd-15-2695-2023	
11	INGV_2003_Talos-Dome_AIR_BM3	INGV	Talos Dome; Queen Mary Land; Terre Adelie	INGV-IT GlacioRadar	https://doi.org/10.5194/essd-15-2695-2023	Filtered out data along 1 manually supplied line due to inconsistencies with surrounding data.
12	KOPRI_UA_2023	KOPRI/UA	Belgica Highlands	UWB IPR	-	
13	NASA_2013_ICEBRIDGE_AIR_BM3	NASA/CRISIS	Operation Icebridge	MCORDS v3	https://doi.org/10.1029/2020RG000712	
14	PRIC_2018_CHA4_AIR_BM3	PRIC	Princess Elizabeth Land (CHA4)	HICARS	https://doi.org/10.5281/zenodo.4023393 https://doi.org/10.5194/essd-12-2765-2020 https://doi.org/10.1038/nature10114	
15	UTIG_1999_SOAR-LVS-WLK_AIR_BM2	UTIG/LDEO	Transantarctic Mountains; South Pole; Lake Vostok; Dome C	SOAR TUD IV (RADgh1 digitizer)	https://doi.org/10.1016/S0012-821X(04)00666-4 https://doi.org/10.15784/601588	Filtered out data along 1 manually supplied line due to inconsistencies with surrounding data.
16	UTIG_2008_ICECAP_AIR_BM2	UTIG/AAD	ICECAP/ Aurora Subglacial Basin	HICARS	https://www.usap-dc.org/EView/dataset/601411 https://doi.org/10.5067/FEEGUT9F089 https://doi.org/10.1038/nature10114	
17	UTIG_2010_ICECAP_AIR_BM3	UTIG/AAD	ICECAP/Antarctic-wide	HICARS	https://doi.org/10.5067/M2KXK0MYN9JG https://doi.org/10.1038/nature10114	Filtered out data within 0.2 km of survey #16 due to inconsistencies. Also filtered out data along 1 manually supplied line due to inconsistencies with surrounding data.
18	UTIG_2016_OLDICE_AIR_BM3	UTIG/AAD	ICECAP/ Dome C	MARFA	https://doi.org/10.15784/601355 https://doi.org/10.1038/nature.2014.0297	

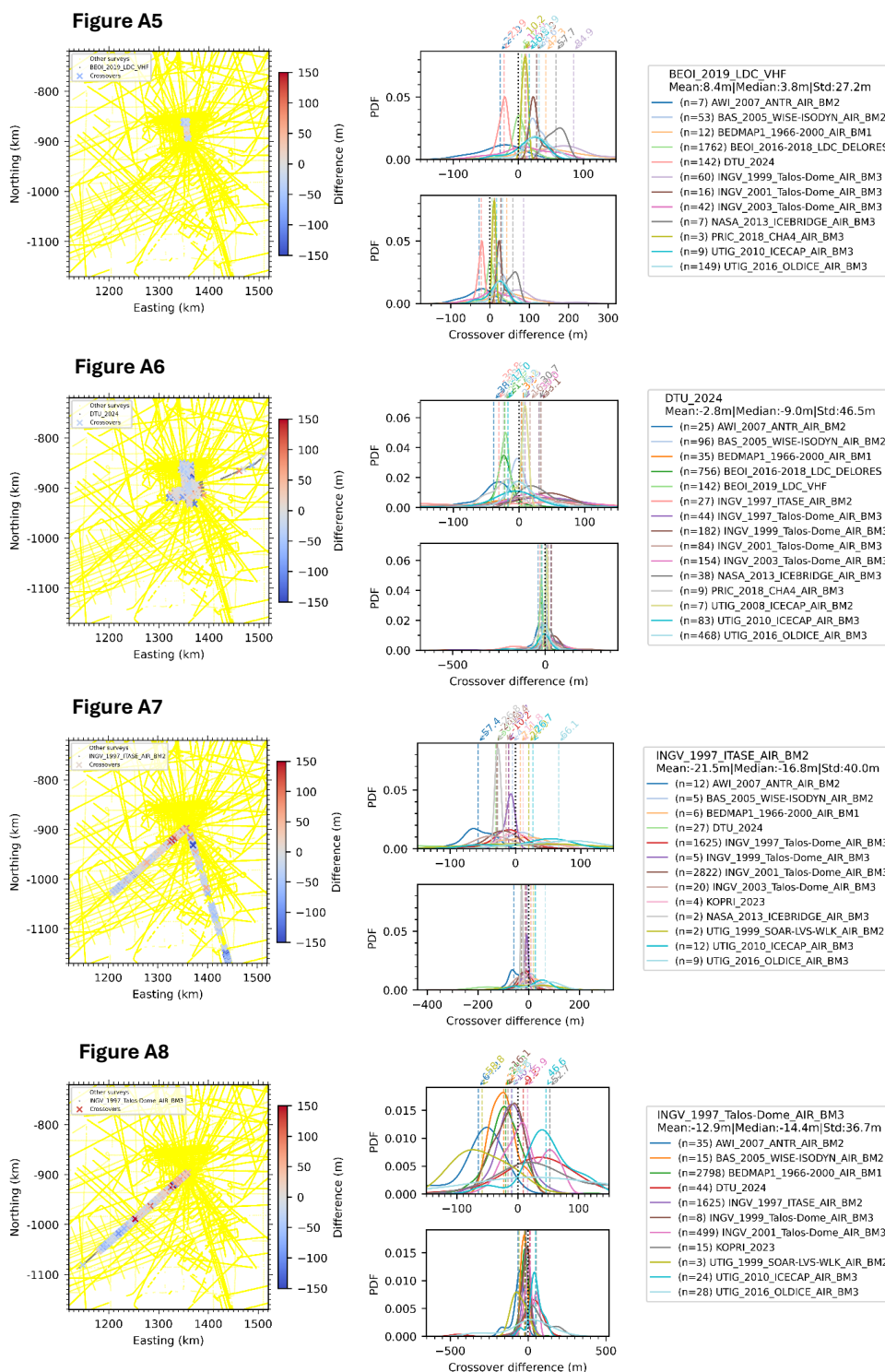


Figures A1-18: Consistency between individual radar surveys and all other surrounding data. Each figure shows a map with 50 m radius crossover points as an X coloured according to the difference in value (Red-Blue colormap). Survey track is shown as a grey line and all other survey tracks are shown as yellow lines. The adjacent histograms show the differences in value between each intersecting survey as a probability density function, with the upper plot showing detailed differences within ± 150 m and lower plot showing the full range of crossover differences. A legend for the histograms is shown to the right with some summary statistics for overall differences between the survey and surrounding measurements





1





2

Figure A9

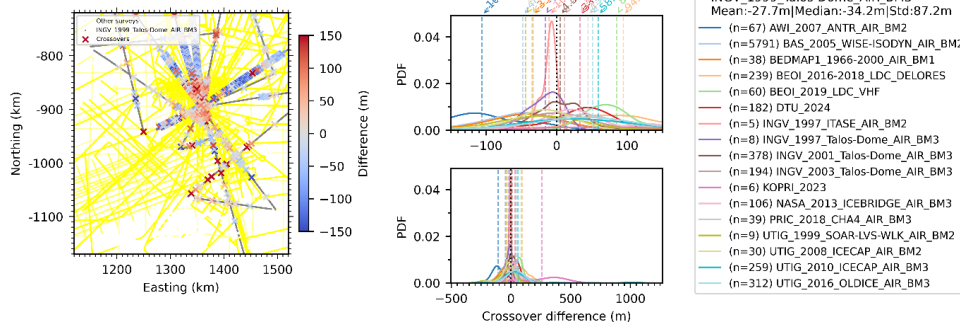


Figure A10

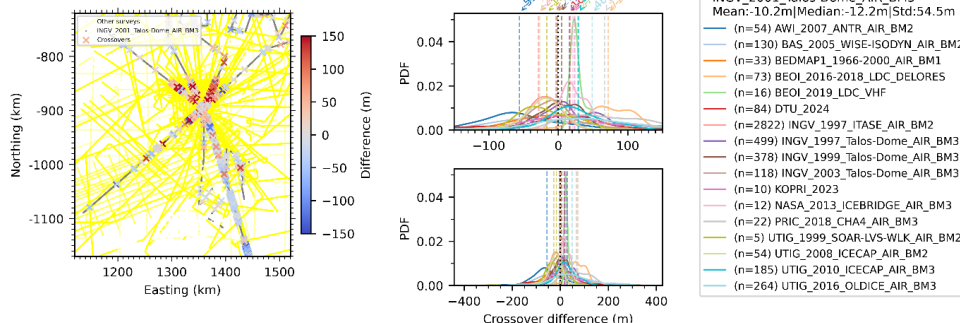


Figure A11

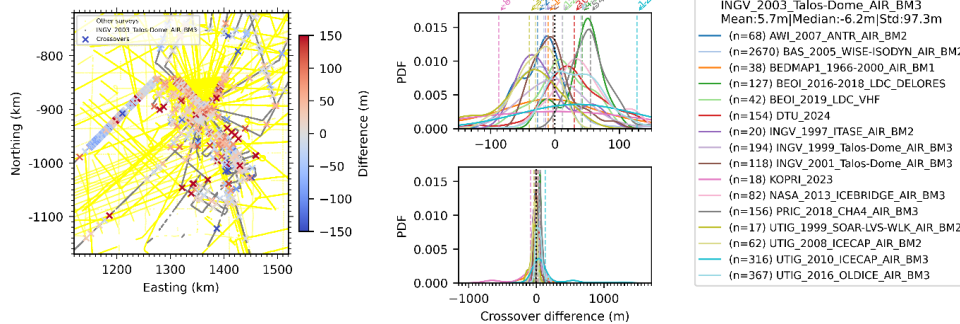
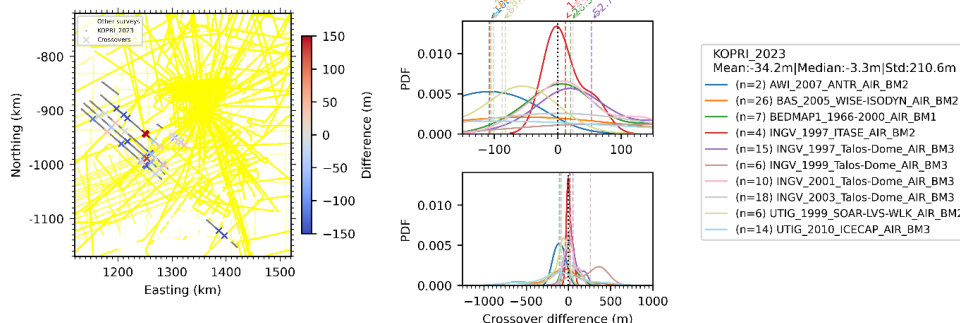


Figure A12





3

Figure A13

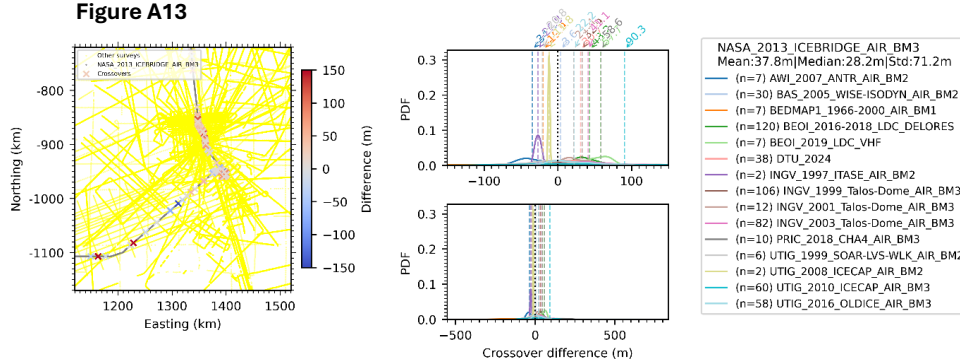


Figure A14

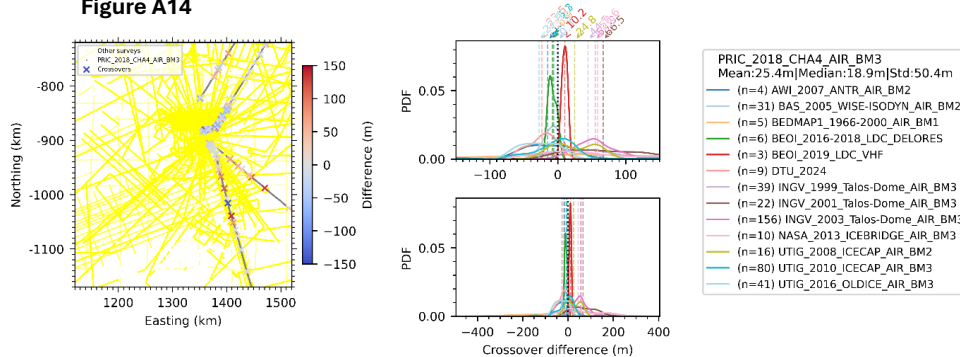


Figure A15

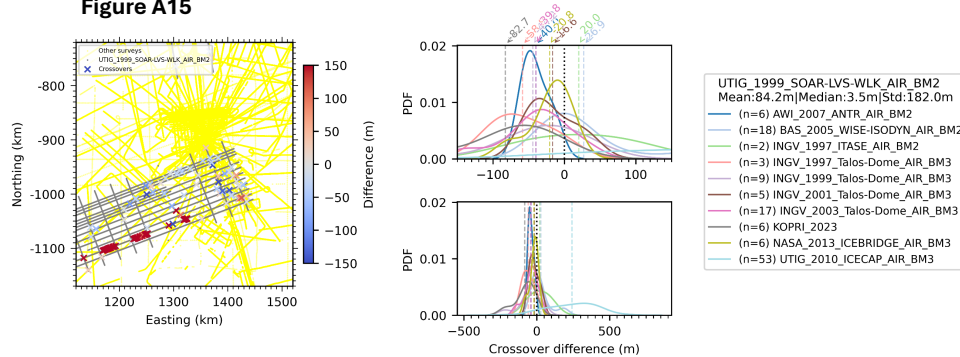
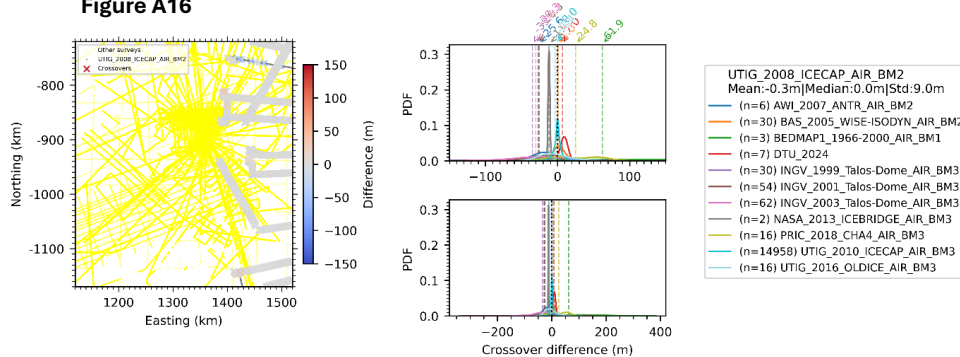


Figure A16





4

Figure A17

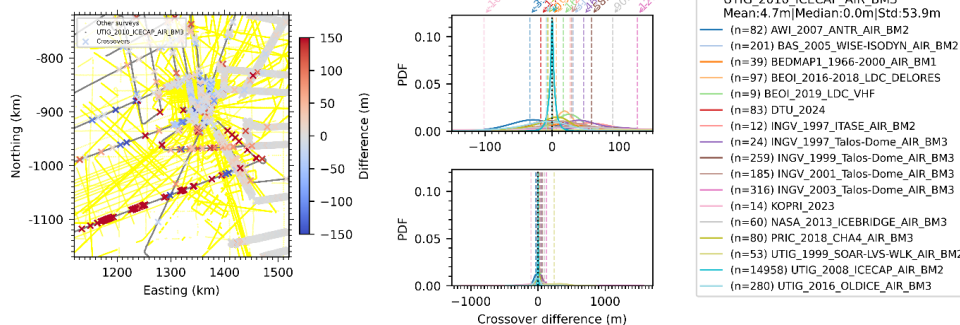


Figure A18

